JOURNAL OF GEOPHYSICAL RESEARCH, VOL. 102, NO. B2, PAGES 3077-3096, FEBRUARY 10, 1997

Dynamics of gas-driven eruptions: Experimental simulations using CO_2-H_2O-polymer system

Youxue Zhang

Department of Geological Sciences, University of Michigan, Ann Arbor

B. Sturtevant

Graduate Aeronautical Laboratories, California Institute of Technology, Pasadena

E. M. Stolper

Division of Geological and Planetary Sciences, California Institute of Technology, Pasadena

Abstract. We report exploratory experiments simulating gas-driven eruptions using the CO_2-H_2O system at room temperature as an analog of natural eruptive systems. The experimental apparatus consists of a test cell and a large tank. Initially, up to 1.0 wt % of CO_2 is dissolved in liquid water under a pressure of up to 735 kPa in the test cell. The experiment is initiated by suddenly reducing the pressure of the test cell to a typical tank pressure of 10 kPa. The following are the main results: (1) The style of the process depends on the decompression ratio. There is a threshold decompression ratio above which rapid eruption occurs. (2) During rapid eruption, there is always fragmentation at the liquid-vapor interface. Fragmentation may also occur in the flow interior. (3) Initially, the top of the erupting column ascends at a constant acceleration (instead of constant velocity). (4) Average bubble radius grows as $t^{2/3}$. (5) When viscosity is 20 times that of pure water or greater, a static foam may be stable after expansion to 97% vesicularity. The experiments provide several insights into natural gas-driven eruptions, including (1) the interplay between bubble growth and ascent of the erupting column must be considered for realistic modeling of bubble growth during gas-driven eruptions, (2) buoyant rise of the bubbly magma is not necessary during an explosive volcanic eruption, and (3) CO_2-driven limnic eruptions can be explosive. The violence increases with the initial CO_2 content dissolved in water.

Introduction

Gas-driven eruptions are powerful and destructive natural hazards. The more familiar type is explosive (the term "explosive" is used hereafter in the generic sense; it does not imply the involvement of shock waves) volcanic eruptions powered by the rapid exsolution of H_2O gas initially dissolved in magma, including the 1991 eruption of Pinatubo, the 1980 eruption of Mount St. Helens that reduced the height of Mount St. Helens by 400 m, and the 79 A.D. eruption of Vesuvius that buried the Roman city of Pompeii. In addition, a new type of eruption has been recently recognized. A massive CO_2 gas release from Lake Nyos, Cameroon, in 1986 killed ~1700 people [*Schenker and Dietrich*, 1986; *Freeth and Kay*, 1987; *Kling et al.*, 1987]. A similar though smaller event occurred at Lake Monoun (also in Cameroon) in 1984, killing ~40 people [*Sigurdsson et al.*, 1987]. Although the origin of the two eruptions is controversial [*Sigvaldson*, 1989], most workers now agree that an eruption of CO_2 gas exsolved from lake water played a role in both events [*Freeth et al.*, 1990]. This gas-charged water eruption in a lake, an internal lake process, has been termed a "limnic eruption" [*Sabroux et al.*, 1990]. *Zhang* [1996] recognized the similarity between H_2O-driven volcanic eruptions and CO_2-driven limnic eruptions in that they are both driven by the rapid exsolution of supersaturated volatile component from a liquid and modeled the dynamics of limnic eruptions. The supersaturation of H_2O in magma can be achieved by crystallization of anhydrous minerals, magma ascent, landslide of overlying rocks, or bubble overpressure [*Steinberg et al.*, 1989a,b]. The supersaturation of CO_2 in lake water can be achieved by gradual leakage of CO_2 into lake bottom water, or some triggering mechanism that moves the nearly saturated bottom water upward. We use the term "gas-driven eruptions" to refer to both types of eruptions.

There have been many theoretical, field, and experimental investigations examining the processes leading to gas-driven eruptions. *Verhoogen* [1951] was the first to discuss the role of bubble growth and rise in eruptions. *Sparks* [1978], *Toramaru* [1989], and *Proussevitch et al.* [1993] simulated bubble growth numerically and emphasized the major role of this process in gas-driven eruptions. *Jaupart and Tait* [1990], *Sparks et al.* [1994], *Cashman and Mangan* [1994], and *Wood* [1995] reviewed physical aspects and dynamics of gas-driven eruptions based on theoretical and experimental work and from textural studies of eruptive products. Using shock-tube techniques, *Kieffer and Sturtevant* [1984] investigated volcanic jets using a one-component gas system, and *Hill and Sturtevant* [1990] and

Paper number 96JB03181.
0148-0227/97/96JB-03181$09.00

Sugioka and Bursik [1995] studied evaporation waves using one-component gas-liquid systems. *Fröhlich* [1987] and *Lorenz et al.* [1994] simulated experimentally the violent interaction between high temperature magma and low temperature water. *Jaupart and Vergniolle* [1988, 1989], *Bagdassarov and Dingwell* [1993], *Thomas et al.* [1994], and *Alidibirov and Dingwell* [1996] studied the formation, stability, deformation, and fragmentation of foams. *Kieffer* [1995] modeled numerically caldera-scale volcanic eruptions on Earth, Venus, and Mars, focusing on the effect of atmospheric pressure in different planetary environments on the development of erupting columns. *Phillips et al.* [1995] carried out an innovative study with a gum rosin-acetone system to simulate the effect of viscosity dependence on the dissolved gas content.

In spite of these and many other studies, the basic physics and chemistry of eruptive processes are not fully understood. A key limitation in our ability to understand volcanic eruptions is the difficulty in observing the dynamics of explosive eruptions from start to finish and at all depths in the volcanic system. Direct observation of active volcanos has provided invaluable information, but there is currently no way to observe the initiation of the eruption at depth or the evolution of the subsurface parts of the volcanic system with time or to measure internal velocities of pyroclastic flows and their volatile and fragmented particle concentrations after emerging at Earth's surface. Although differing in scale and complexity from natural eruptions, laboratory simulations provide an alternative to direct observations of natural systems. In this paper we report experimental simulations of gas-driven eruptions using the simple system CO_2-H_2O at room temperature as a model and show that eruptions can be produced under suitable conditions [*Mader et al.*, 1994]. Our experimental study differs from previous ones [*Kieffer and Sturtevant*, 1984; *Hill and Sturtevant*, 1990; *Sugioka and Bursik*, 1995] in that we generate eruptions by rapid supersaturation of dissolved gas in a binary gas-liquid solution. We examine several aspects of the eruption processes, including nucleation, growth, and coalescence of bubbles; expansion of the bubbly flow; formation, stability, and fragmentation of foams; and eruption dynamics. High-speed motion picture photography has been used to capture simultaneously the details of all these processes. The experiments, although still only exploratory, suggest some simple "laws" for the dynamics of eruptions and bubble growth.

Experimental Approach and Techniques

Our experiments simulate the exsolution of volatile components from a liquid roughly uniformly supersaturated with respect to a gas phase, the expansion of the gas-liquid system, and two-phase flow that occurs in the conduit and near the vent of an eruption. The experiments consist of a nearly instantaneous decompression of CO_2-saturated water, which, having become abruptly supersaturated with respect to CO_2, exsolves rapidly expanding bubbles, which in turn lead to a variety of simulated eruptive phenomena. By observing the sequence of depressurization, bubble growth, and eruption in these experiments using high-speed photography, we are able to evaluate both qualitatively and quantitatively a range of phenomena that are thought to occur in natural gas-driven eruptions but are not readily observable. The objectives are to elucidate the processes that control volume expansion and eruption and to quantify the conditions under which an explosive eruption occurs and the dynamics of the eruption process.

Choice of an Analog System

A key feature of natural explosive volcanic eruptions and lake eruptions is the rapid growth of bubbles when the gas-liquid solution becomes supersaturated with respect to the gas phase. This growth can reflect both diffusion of dissolved volatiles (largely H_2O and/or CO_2) from the liquid phase into the bubbles and expansion of preexisting bubbles due to depressurization. After eruption, the volatile components, initially wholly or partially dissolved in the liquid phase, are nearly entirely in the gaseous state. Although most of the volume of the system after the eruption is occupied by the exsolved gas, the liquid phase still makes up most of the mass of the system. To model these features of natural eruptions, experiments were conducted on a two-component system under conditions at which one component (H_2O) is a stable liquid and the other (CO_2) is a stable gas (Figure 1). Other desirable features of the CO_2-H_2O system include its nontoxicity, the transparency of liquid H_2O-CO_2 solutions, and the fact that the properties of the CO_2-H_2O system are well known. In addition, laboratory simulations of eruptions using this system are useful in elucidating mechanisms and dynamics of CO_2-driven limnic eruptions [*Freeth and Kay*, 1987; *Kling et al.*, 1987].

The CO_2-H_2O-Polymer System

The viscosity, surface tension, and vapor pressure of liquid H_2O, the vapor pressure of liquid CO_2, and the solubility and diffusivity of CO_2 in water at 20°C and 25°C (the temperature range of our experiments) are given in Table 1. The surface tension of water is about 1/5 that of magmatic liquids [*Walker and Mullins*, 1981]. The diffusivity of CO_2 in water at 25°C is 1.92×10^{-9} m^2/s, 250 times that of molecular H_2O in rhyolitic magma at 850°C (7.5×10^{-12} m^2/s [*Zhang et al.*, 1991]). The partial molar volume of CO_2 in water is 32.3×10^{-6} m^3/mol based on the dependence of solubility on pressure [*Weiss*, 1974]. Hence a CO_2-H_2O solution with 1.0 wt % dissolved CO_2 has a density ~0.3% higher than that of pure water. The phase diagram of the CO_2-H_2O system at 25°C calculated from the solubility data (Figure 1) shows a large two-phase region (CO_2 vapor plus H_2O liquid) between 0.03 and 62 atm (3 kPa and 6.3 MPa).

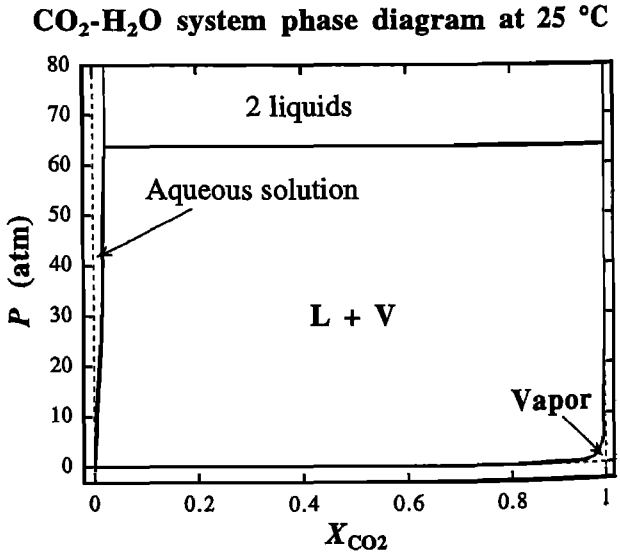

Figure 1. Phase diagram of the CO_2 - H_2O system at 25°C calculated using solubility data of *Wiebe and Gaddy* [1940].

Table 1. Selected Properties of CO_2 - H_2O System

	Pure H_2O				Pure CO_2	CO_2 in H_2O	
T, °C	Viscosity, mPa s	Surface Tension, N/m	Density, kg/m^3	Vapor Pressure, kPa	Vapor Pressure, MPa	Solubility, λ*	Diffusivity, m^2/s
20	1.00	0.0729	998.2	2.338	5.70	0.94	—
25	0.89	0.0721	997.0	3.167	6.38	0.83	1.92×10^{-9}

Data from *Dean* [1985], except CO_2 vapor pressure from *Weast* [1983] and diffusivity of CO_2 in water from *Cussler* [1984].

*The solubility is Ostward solubility (λ), given by volume of total CO_2 at the T and P absorbed by unit volume of water, which is the same as the concentration of CO_2 dissolved in water in mol/m^3 divided by that of CO_2 in the gas phase at the T and P ($\lambda = C^{\text{liquid phase}}/C^{\text{gas phase}}$). The CO_2 gas is assumed to be ideal under experimental conditions.

Table 2 lists equilibrium constants for the reactions involving the most abundant carbon-bearing species (CO_2 molecules, H_2CO_3, HCO_3^- and CO_3^{2-}) in an aqueous solution. Using these equilibrium constants, the concentrations of the species have been calculated for several P_{CO_2} at 25 °C (Table 3). For a CO_2 partial pressure greater than 0.1 MPa, more than 99% of total CO_2 dissolved in water is molecular CO_2. Therefore, in our experiments (with initial pressure of 0.3 to 0.7 MPa), most of the dissolved CO_2 is molecular CO_2 prior to depressurization and vapor exsolution. Because the dissolved molecular CO_2 is the ingredient for bubble growth, the kinetics of interconversion reactions among the species do not play an important role in our decompression experiments. For experiments in which CO_2 molecules are supplied by the reaction between acid and carbonate solutions, reaction kinetics may play a role [*Mader et al.*, 1994, 1996].

A potentially significant difference between our simulations and natural magmas is that natural systems are much more viscous than liquid water [Shaw, 1972]. In order to examine the effect of viscosity on our simulations, up to 1.0 wt % of an organic polymer is added to the aqueous solution in some experiments to increase its viscosity. Four types of polymers are used (Natrosol® hydroxyethylcellulose GR, KR, HR, and HHR provided by the Aqualon Company). The polymers increase the viscosity of water by a factor of 5 to 700, depending on the type and amount of polymer used. The viscosity of the polymer-bearing aqueous solution is estimated from a chart supplied by the manufacturer and was confirmed by direct measurement. The surface tension of the solution is determined to be lower than that of pure water by (10±3)% at 1.0 wt % polymer for all polymers. The addition of polymer has no noticeable effect on the solubility of CO_2 in water. The effect of polymer addition on CO_2 diffusivity in water has not been determined and is assumed to be negligible.

Experimental Techniques and Procedures

The experimental apparatus comprises mainly a test cell and a tank (Figure 2) [*Hill and Sturtevant*, 1990]. The test cell is an analog of the magma chamber and the volcanic conduit and is filled with water that is saturated with up to 735 kPa of CO_2. Several cylindrical test cells of different lengths (Table 4) used in this work have a 25.4 mm inner diameter, smooth walls, and a rated pressure limit of 700 kPa. The test cell size is chosen such that it is much larger than the largest bubble to form during the early phases of eruption. The tank (with an ID of 0.61 m and a height of 0.91 m) is an analog of the open atmosphere into which the volcano erupts. Its volume is over 800 times that of the longest test cell (typical tank pressure rise over the course of an experiment is less than 10% of the initial tank pressure). Prior to each experiment, the tank is evacuated to a pressure, P_{tank}, of typically 6.9 to 24 kPa (Table 4). Since our purpose is to examine the exsolution of a gas from a liquid, this pressure has to be greater than the vapor pressure of water (2.34 kPa at 20 °C and 3.17 kPa at 25 °C), or the water would not remain in liquid form after depressurization. Several experiments were run to examine what happens when P_{tank} was lower than the vapor pressure of water (experiments 71 and 86 in Table 4, plus some others not included in Table 4). The decompression ratio, the ratio of the saturation pressure (i.e., pressure in the test cell prior to depressurization by opening it to the tank) to the ambient pressure (i.e., pressure in the tank prior to depressurization of the test cell), ranges from 2.5 to 300.

The test cell is filled with a CO_2-saturated solution to a desired pressure in the following way. The water is first equilibrated with CO_2 vapor in a 0.5×10^{-3} m^3 metal cylinder (the cylinder was shaken to assure a uniform CO_2 concentration in the liquid phase) at a relatively high pressure, P_0 (e.g., 1 MPa). Before filling the test cell with the solution, the test cell and the

Table 2. Reactions in CO_2 - H_2O Solution

Reaction	K Expression	K at 25°C	Ref.
$CO_2(\text{vapor}) = CO_2(\text{aq})$	$\frac{[CO_2]_{aq}}{[CO_2]_{gas}} = \lambda$	0.83*	1
$CO_2(\text{aq}) + H_2O = H_2CO_3$	$\frac{[H_2CO_3]}{[CO_2]_{aq}}$	0.0025	2
$H_2CO_3 = H^+ + HCO_3^-$	$\frac{[H^+][HCO_3^-]}{[H_2CO_3]}$	$10^{-3.76}$	2
$HCO_3^- = H^+ + CO_3^{2-}$	$\frac{[H^+][CO_3^{2-}]}{[HCO_3^-]}$	$10^{-10.33}$	2

Molecular CO_2 are present in both the vapor and the aqueous phase, and hence the phase is indicated. All other species shown are in the aqueous phase. All concentrations are in moles per liter.

References are:1, *Dean* [1985, p. 10-4]. The data of *Dean* [1985] are for total CO_2 dissolved in water, which at 0.1 MPa is different from molecular CO_2 dissolved in water only by a negligible amount (less than 1% relative); 2, *Dean* [1985, p. 5-14].

*K at 20°C is 0.94.

Table 3. Species Concentrations at 25°C in CO_2 - H_2O Solution

P_{CO_2}, MPa	$[CO_2]_{aq}$, mol/L	$[H_2CO_3]$, mol/L	$[HCO_3^-]$, mol/L	$[CO_3^{2-}]$, mol/L	*p*H
$3x10^{-5}$	$1.00x10^{-5}$	$2.5x10^{-8}$	$2.1x10^{-6}$	$4.7x10^{-11}$	5.7
0.01	0.0033	$8.4x10^{-6}$	$3.8x10^{-5}$	$4.7x10^{-11}$	4.4
0.1	0.033	$8.4x10^{-5}$	$1.21x10^{-4}$	$4.7x10^{-11}$	3.9
0.2	0.067	$1.67x10^{-4}$	$1.71x10^{-4}$	$4.7x10^{-11}$	3.8
0.4	0.134	$3.3x10^{-4}$	$2.4x10^{-4}$	$4.7x10^{-11}$	3.6
0.6	0.20	$5.0x10^{-4}$	$3.0x10^{-4}$	$4.7x10^{-11}$	3.5
0.8	0.27	$6.7x10^{-4}$	$3.4x10^{-4}$	$4.7x10^{-11}$	3.5

Equilibrium constants used in the calculations are from Table 2.

tube line connecting the metal cylinder and the test cell are evacuated, then pressurized with CO_2 gas from the metal cylinder to a pressure, P_1 (e.g., 500 kPa), which is somewhat lower than the target pressure. (At this time, the pressure in the metal cylinder is slightly less than P_0.) The CO_2-H_2O is then allowed to flow into the test cell from the metal cylinder, driven by the pressure difference between them (i.e., $P_0 > P_1$). Note that because $P_0 > P_1$, the pressure in the metal cylinder decreases when it is exposed to the test cell (and the pressure in the test cell increases) and CO_2 exsolves from the solution as the solution flows into the test cell. When the pressure in the test cell has risen to ~20% above the target pressure, part of the gas in the test cell is pumped out to return the pressure to near P_1. This procedure is repeated until the desired amount of solution has entered the test cell. The final pressure is typically about 10% higher than P_1. We then allow the solution and the vapor in the test cell to equilibrate for 10 min to 24 hours. We rely on convection in the solution to help rehomogenize the solution after it enters the test cell, but this has not been quantified. The concentration of CO_2 in the solution prior to depressurization in the experiments is estimated by assuming equilibrium of the solution with the gas in the test cell, but the actual concentration of CO_2 in the solution may vary somewhat due to incomplete homogenization of the solution in the test cell. In particular, early experiments (i.e., with experiment numbers less than 100) may have suffered more from this problem because the filling procedure was improved at this point in the sequence of experiments.

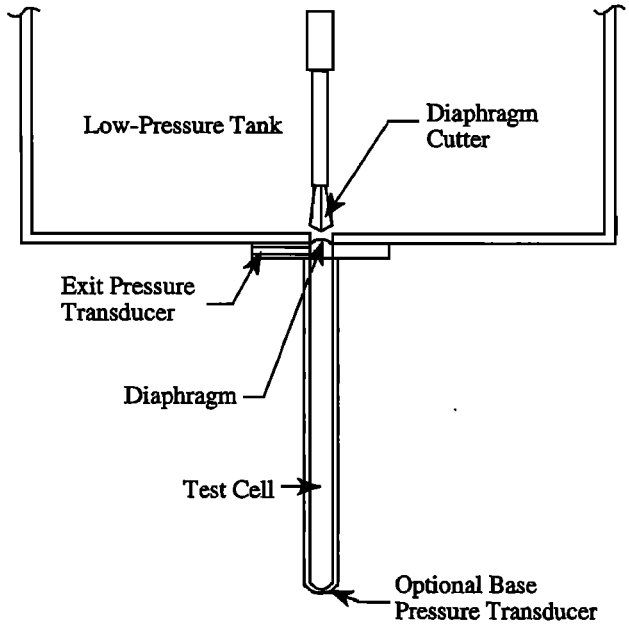

Figure 2. A sketch of the experimental apparatus. Test cell and tank pressures are measured before and after the experiment with precision dial gauges.

The experimental procedure after filling the test cell with solution follows that of *Hill and Sturtevant* [1990]. Each experiment is initiated by rupturing a diaphragm separating the test cell and the tank using a pneumatically driven knife inside the tank (Figure 2). The cutting resulted in cross-shaped slits through the Al diaphragm. Owing to a higher pressure in the test cell than in the tank, the diaphragm is completely opened by the gas flow.

The subsequent process is recorded with video at 30 frames per second (fps) and high-speed motion picture photography. The high-speed films are taken at nominal speeds of 1000 to 4000 fps with a 16-mm Hycam II camera (Redlake Corporation, Morgan Hill, California). In some experiments, the speed was calibrated using a timer that pulses every millisecond. On the basis of these calibrations, the accuracy of the nominal speed is ~5% and the precision is ~3%. (All uncertainties quoted in this paper are at the 2σ level.) For example, in experiment 149, the nominal speed is 4000 fps, but the actual speed is 4120 fps to 4200 fps. Reported experimental time is nominal time.

Because heat diffusion is rapid compared to the distance scale between bubbles (typically ≤0.1 mm in the foam stage) but slow compared to the diameter of the whole column (25 mm), the process is roughly adiabatic in terms of the mixture (instead of each phase). Owing to the large heat capacity of water, the temperature decrease of water due to adiabatic exsolution of CO_2 from water is very small (estimated to be less than 3°C). Hence the process is also roughly isothermal. Besides static measurement of pressures in the test cell and in the tank in all experiments (reported in Table 4), pressure variations at the top and bottom of the test cell (exit and base pressures) are measured for some experiments with quartz piezoelectric transducers (response times of 1 μs) (Figure 2) and recorded on a digital oscilloscope (Nicolet 4094) at 25,000 readings per second. Based on calibrations we performed, the transducer that measures the base pressure has a precision of 0.4%, and the one that measures the exit pressure has a precision of 1.4% of the maximum pressure. The accuracy is probably no better than 5%,

which limits our ability to measure the small differences between the decompressed base and exit pressures.

Table 4 summarizes the conditions for all experiments for which data were obtained from high speed motion pictures; it excludes experiments such as those examining the eruption threshold for which high speed motion pictures were not taken. The motion picture images were examined frame by frame for the dynamics of the bubbly flow and the nucleation and growth of bubbles.

Experimental Results

General Description

A range of processes have been observed, depending on the experimental conditions. At one extreme, when the initial P_{cell}/P_{tank} is small (≤2), there is quiet exsolution (i.e., diffusive loss of CO_2 without bubbling) and occasional bubbling with little or no measurable change in the liquid column after rupture of the diaphragm. At the other extreme, when the initial P_{cell}/P_{tank} is large (≥50), bubbles nucleate and grow rapidly and accelerate the liquid column upward in an eruption. For the purposes of this study, an eruption is defined as an event in which a measurable amount of liquid is ejected from the test cell. Merging or coalescence of bubbles is defined as the combination of two or more bubbles into fewer and larger bubbles. Fragmentation is defined as the rupture of bubble walls into small droplets without reformation of a larger bubble so that the gas becomes a continuous phase (instead of individual bubbles). A foam is defined as a system in which roughly uniformly distributed bubbles make up more than 74% of the volume [*Cashman and Mangan*, 1994] but the liquid is still a continuous phase. A stable foam is defined as a foam that does not fragment on the timescale recorded by films (i.e., several hundred milliseconds) except for at the flow front, which always fragments during an eruption to some extent.

As can be established from gas dynamics theory, after the rupture of the diaphragm the gas overlying the liquid rushes through the opening at sonic velocity, producing a weak shock wave propagating from the exit into the tank. The gas in the test

Table 4. Experimental Conditions

Experiment	T, °C	P_{tank}, kPa	P_{cell}, kPa	TCType	$h_{f,0}$, m	Polymer added type, %	η, Pa s	Film speed, fps	Field of view, mm
67	21.0	6.3	525	S	0.110	none	0.001	2000	190
68	22.0	6.9	654	S	0.113	none	0.001	2000	190
69	22.0	6.9	479	S	0.093	none	0.001	1000	190
70	22.0	6.9	335	S	0.094	none	0.001	1000	190
71*	22.2	2.5	681	S	0.101	GR (0.5%)	0.005	1000	190
72	21.7	6.9	512	S	0.124	GR (0.5%)	0.005	1000	190
77	21.8	10	622	S	0.077	KR (0.5%)	0.017	1000	190
78	20.6	6.3	430	S	0.088	KR (0.5%)	0.017	2000	190
80	21.5	10	562	S	0.125	HR (0.7%)	0.70	2000	190
83+	22.9	6.9	565	S	0.098	none	0.001	4000	85
84	23.4	6.9	483	S	0.049	none	0.001	3000	190
85	23.4	10	618	S	0.034	KR (0.5%)	0.018	3000	190
86*	22.0	~2.1	621	S	0.076	KR (0.5%)	0.018	3000	190
87	21.3	21	624	S	0.114	KR (0.5%)	0.018	3000	190
88	24.0	6.9	214	S	0.083	KR (0.5%)	0.018	3000	190
89+	22.2	11	496	S	0.084	KR (0.5%)	0.018	4000	33
90+	21.0	7.2	524	S	0.085	GR (0.5%)	0.005	4000	33
91	24.0	6.9	403	S	0.066	GR (0.5%)	0.005	3000	190
92	22.0	24	735	S	0.086	KR (1.0%)	0.16	3000	190
93	21.5	6.2	235	S	0.084	KR (1.0%)	0.16	3000	190
94‡	20.5	---	487	S	0.110	KR (1.0%)	0.16	4000	33
143‡	21.2	6.9	565	L1	0.105	none	0.001	4000	40
145‡	22.8	6.9	565	L1	0.104	none	0.001	4000	29
147‡	19.7	6.9	565	L1	0.104	none	0.001	4000	29
148‡	19.6	6.9	565	L1	0.098	none	0.001	4000	100
149	19.8	6.9	558	L1	0.104	none	0.001	4175	160
150+	19.7	6.9	567	L1	0.106	none	0.001	4000	60
152+	19.3	6.9	563	L1	0.095	none	0.001	4000	54

Only experiments with high-speed motion picture images are reported. TC (test cell) type, all test cells are cylindrical and have an inner diameter of 25.4 mm. L1 is a tube with length of 0.456 m; L2 is a tube with a length of 0.610 m; S is a tube with a length of 0.254 m and with glass bottom (i.e., it cannot accept a transducer). Film speed is in frames per second (fps). The field of view is given along the length of the test cell. The resolution approaches 1/300 times the field of view.

*P_{tank} is too low so that water also vaporizes.

+Close-up shot. The total field of view (last column) gives an indication of the resolution.

‡Close-up shot and initial front is not in the view. Experiment 94 is a close-up shot of the bottom; experiments 143-148 are close-ups of the upper part of the test cell above the initial solution; the front moves into view. We initially thought that front acceleration may be derived from such data, but due to the fragmentation of the front, it is difficult to obtain front acceleration accurately.

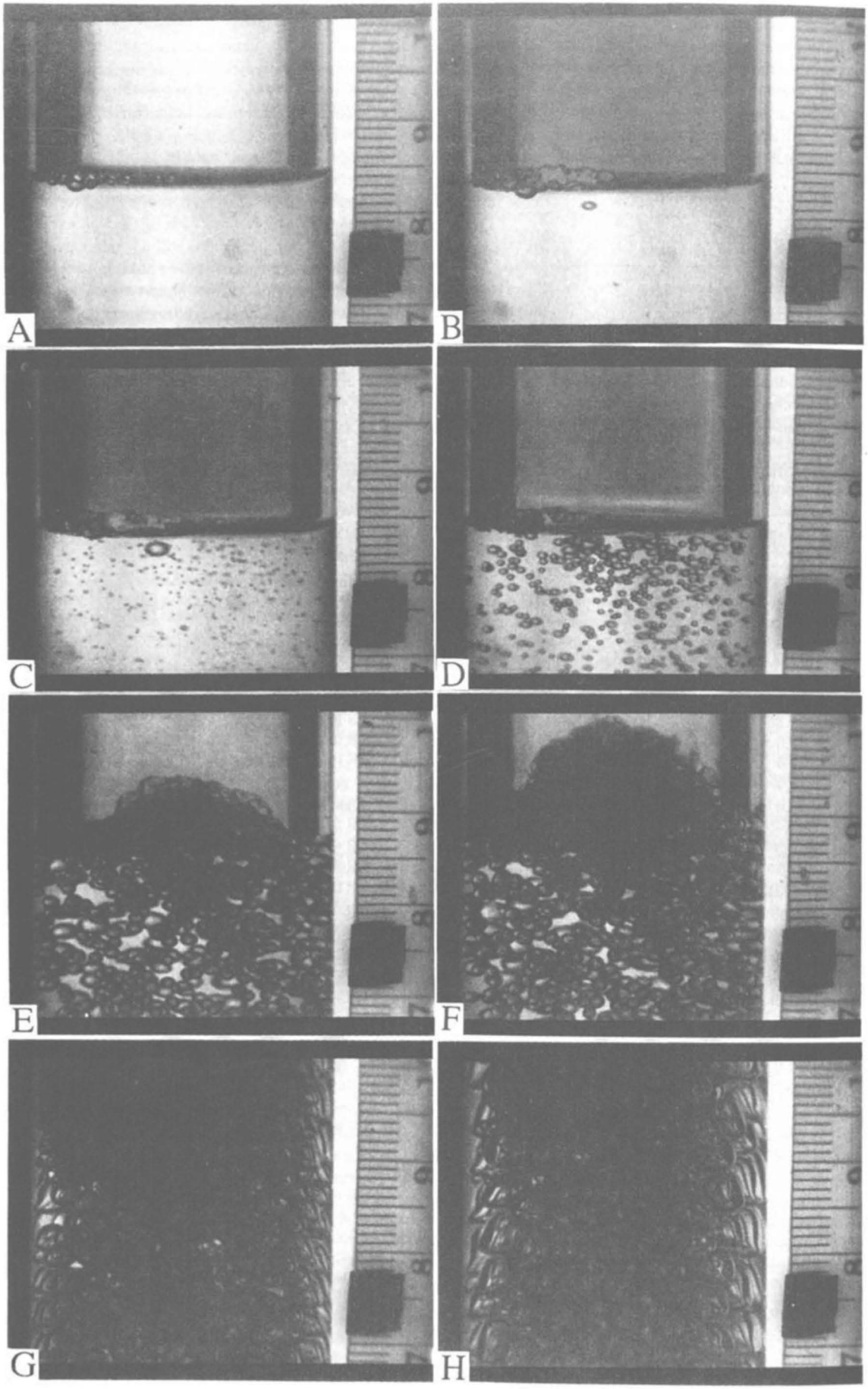
A
B
C
D
E
F
G
H

cell depressurizes in a nonsteady rarefaction wave that reverberates between the surface of the liquid and the exit, bringing the vapor-phase pressure first rapidly, then more slowly down to the tank pressure. The reflection of the rarefaction wave at surface of the liquid is partial; That is, the rarefaction wave also propagates into the liquid. Owing to the high sound speed in the liquid, the pressure at the bottom responds nearly instantaneously to the pressure at the interface, although preexisting bubbles can increase the compressibility of the liquid and retard the pressure response. There are also reflections of the shock wave upon reaching the top of the tank (0.9 m above the diaphragm), but these are strongly attenuated in the large-volume tank. The complete depressurization with reverberations takes ~10 ms, after which the pressure in the liquid is the same as the tank pressure plus the pressure due to the weight of the overlying liquid (0.98 kPa at the base of a 0.1 m liquid column) plus a pressure thrust (discussed below). As the gas-saturated column of liquid depressurizes, bubbles nucleate and grow. If the degree of supersaturation is high enough, bubbles grow so rapidly that an expanding column of gas plus liquid moves upward through the test cell as a two-phase, bubbly flow. When viewed at each stage of the expansion on a length scale greater than individual bubbles or droplets, the flow away from the wall is roughly uniform across the diameter of the test cell.

When the solution is highly supersaturated, bubbles appear several milliseconds after the initiation of the depressurization, forming roughly simultaneously and uniformly throughout the bulk of the liquid. The bubbles all grow at approximately the same rate. When the solution is only slightly supersaturated and eruptions do not occur, bubbles nucleate on the test cell wall, probably heterogeneously at asperities, and a column of bubbles rises from each nucleation site.

When the number density of bubbles (N) is small, shapes of individual bubbles can be seen in close-up shots, but they are difficult to see when N is large. Bubbles are initially spherical and then become oblate with the short axis oriented vertically due to buoyant rise in the high-acceleration field (the maximum ratio of the long to the short axis is ~2; reported diameter for these bubbles is the geometric average diameter). At the end of an eruption, bubbles "touch" without coalescence or fragmentation in a foam, and they exhibit roughly equidimensional polyhedral shapes.

Most of the phenomena described in the previous paragraphs are readily visible in the high speed motion picture images. Several films have been transferred to a video tape that has been deposited with the AGU publication office[1]. Some frames of the films have been transferred to photos and are briefly described here and shown in Figures 3-7.

Figure 3 shows close-up shots (4000 fps) of the initial front of the erupting column for experiment 89. The viscosity of the solution is 0.018 Pa s. Individual bubbles can be seen (Figures 3d-3h), indicating a low number density of initially well-separated bubbles. As bubbles grow, the vesicularity (volume fraction of bubbles) increases to more than 74%. At the front bubbles merge and fragment. Lower in the flow, as seen later from the same view point after the flow has expanded, bubbles do not merge or fragment; instead, they deform into polyhedral shapes and form a stable foam. In Figure 3h the fluid in the viewing window was initially 14 to 20 mm above the bottom of the test cell, and so experienced only small acceleration and velocity. Throughout the experiment, the two-phase bubbly flow is roughly uniform.

Figure 4 shows photos (2000 fps) for polymer-free experiment 84. The whole test cell is in the field of view. The viscosity is 0.001 Pa s. The bubbly flow fragments first at the interface and forms a mist. Fragmentation propagates downward into the developing bubbly flow until finally only bubbling fluid remains in the test cell after the eruption. No stable foam developed.

Figure 5 shows photos of experiment 80 (2000 fps). The whole test cell is in the field of view. The viscosity of the

[1]High speed motion picture images on videotape are available by mail from AGU, 2000 Florida Avenue, N.W., Washington, DC 20009 or by phone at 800-966-2481; $25.00. Product code 96JB0318V. Payment must accompany order.

Figure 3. (opposite) A sequence of photos before and after the initiation of experiment 89 (η = 0.018 Pa s; close-up shot focusing at the front; 4000 fps) from the high-speed motion picture images. (a) Before experiment, both the liquid phase (lower part) and the vapor phase are clear. The ruler at the right hand side of the test cell indicates the scale (each small division is 1 mm). Initial front height is 83.7 ± 0.5 mm. There are some bubbles at the liquid-vapor interface. These bubbles do not affect the processes in the interior of the erupting column. However, they do affect the front height measurement when there are many of them because the bubbles expand as the pressure is suddenly reduced. (b) At t = 0.75 ms, the vapor phase above the solution is darkened (fog). Bubbles have not formed yet. All experiments show darkened clouds (often oscillating) before or simultaneously with bubble formation. We define t = 0 to be the frame right before the first appearance of these darkened clouds because we have no other way to tell the rupture of the diaphragm. In other figures we do not show the picture before the experiment and the picture with dark clouds. (c) At t = 2.5 ms, individual bubbles in the solution are clearly present and roughly randomly distributed. The first appearance of bubbles is at 1.75 ms. The incubation time (t_0) by fitting front height ascent data is 1.9±1.2 ms, consistent with the observation of bubble appearance. (d) At 6 ms, bubbles are bigger and most of similar size. The front has risen to 84.5±0.5 mm due to bubble growth. The instantaneous front ascent velocity (v_f) is ~0.1 m/s. The instantaneous ascent velocity of other layers is proportional to their height. Though not clear from the pictures, the motion pictures show that the front height rises in a oscillating fashion due to a reverberating wave. (e) At 25 ms, the front is convex up and fragmenting. The average front has risen to 91±1 mm ($v_f \approx$ 0.65 m/s; v at 84 mm height is ~0.6 m/s). Most bubbles are slightly oblate with short axis along the vertical axis. (f) At 32.5 ms, the front reaches 96.5±1.5 mm and is moving out of the view ($v_f \approx$ 0.86 m/s; v at 84 mm height is ~0.75 m/s). The upper 7 mm of the flow is fragmented. (g) At 100 ms, bubbles are still spherical and slightly oblate and well separated from one another (though they appear to be close due to bubbles behind bubbles). The interaction of bubbles may act to reduce the oblateness of bubbles. Uniform bubbly flow is well developed. Average bubble diameter is 2.6±0.2 mm. (h) At 200 ms, polygonal bubbles form a stable foam. Average bubble diameter is 4.2 ± 0.3 mm. The foam is stable at the end of the film (363 ms) and the average diameter of polygonal bubbles has increased to 6.2±0.4 mm.

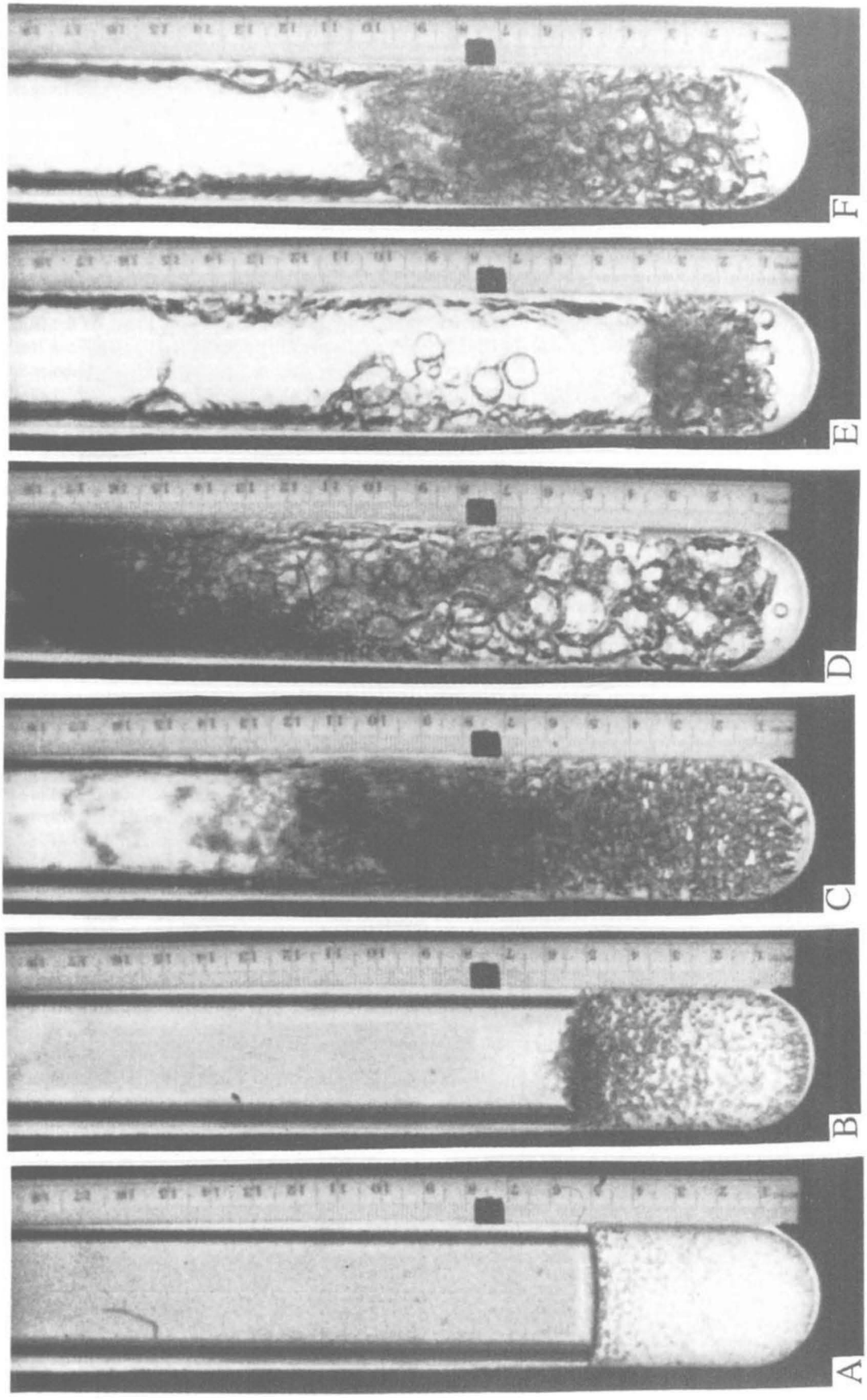

Figure 4. A sequence of photos for experiment 84 (η = 0.001 Pa s; polymer-free; the whole test cell in the view; 3000 fps). (a) At t = 5 ms, bubbles are visible. The height of the front is still at the initial height 49 mm, reflecting a low number density of bubbles. (b) At 10 ms, the front has risen to 55±1.5 mm. The upper 6 mm of the column is fragmented into a fine spray. (c) At 35 ms, the front is not easily defined and the front height versus time curve cannot be accurately measured. (d) At 100 ms, the bottom 8 mm layer of the column is almost free of bubbles. No stable foam is formed. (e) At 200 ms, spherical droplets of liquid are falling back. Another eruption is just starting. (f) At 240 ms, the second eruption rises to 103 mm. Two more such secondary eruptions followed

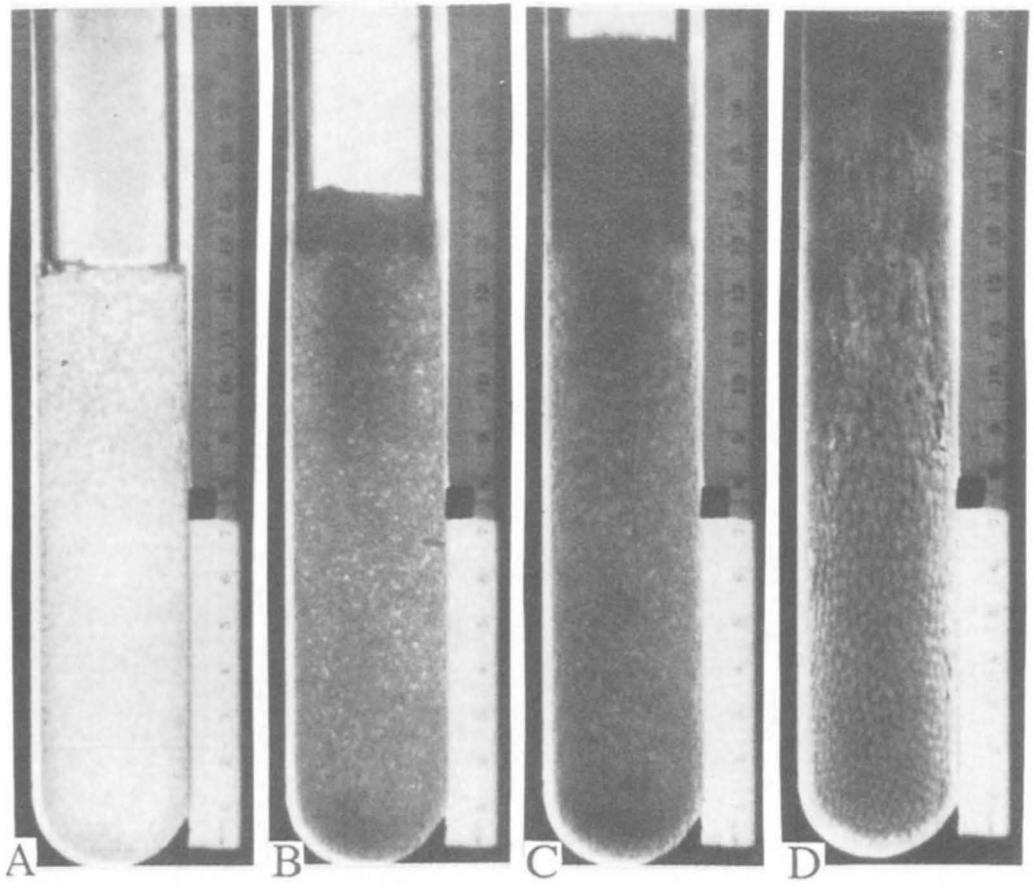

Figure 5. A sequence of photos for Experiment #80 (viscosity η = 0.7 Pa s; 2000 fps; h_0 = 125 mm). (a) At t = 5 ms, bubbles are present. Though bubbles are small, the front height has increased to h_f = 126.5±1.0 mm with $v_f \approx$ 0.7 m/s, indicating a high number density of bubbles. (b) At 17 ms, the front reaches 140 mm ($v_f \approx$ 2.5 m/s, and v at 126.5 mm height is ~2.3 m/s). (c) At 28 ms, the front is flat and reaches 175 mm ($v_f \approx$ 4.2 m/s, and v at 125 mm height is ~3.0 m/s). The upper 40 mm of the column is darker. (d) At 220 ms, individual polygonal bubbles can be seen in the lower 70 mm of the column and form a stable foam.

solution is 0.70 Pa s (the highest viscosity solution used in our experiments). Fragmentation occurs at and near the free surface. Bubbly flow is well developed in the interior of the column after ~30 ms of bubble formation and growth.

Figure 6 shows close-up shots (4000 fps) of the bottom 30 mm of the column for experiment 94. The viscosity of the solution is 0.16 Pa s. In the early stage, bubbles form uniformly in the column. In the late stage, the lower 10 mm of the column is almost free of bubbles due to buoyant rise.

Figure 7 shows photos for experiment 86 (3000 fps). The viscosity of the solution is 0.018 Pa s. This experiment examines a case in which the tank pressure (~2.1 kPa) is lower than the vapor pressure of water (2.64 kPa). The initial eruption behavior is similar to that in other experiments. Fragmentation occurs because a foam is not stable (liquid water at the bubble walls vaporizes). After the eruption, no individual bubbles can be seen and a mist is left in the test cell.

Exit and Base Pressures

Figure 8 shows exit and base pressure vs. time for two experiments. Within the first millisecond, as the gas rushes from the test cell into the tank, the exit pressure, P_{exit}, decreases to ~30% of the initial pressure and stays roughly constant for the next 2 ms as the rarefaction wave propagates downward. After the rarefaction wave has reflected from the gas-liquid interface and returned to the exit, the exit pressure decreases gradually to a minimum pressure (often indistinguishable from zero due to uncertainties in the calibration of the transducer) in ~10 ms. The exit pressure then increases slightly, which is an artifact due to the recovery of the transducer. In contrast to the exit pressure, the base pressure, P_{base}, evolves smoothly. It starts to decrease ~1.3 ms after the exit pressure starts to decrease (reflecting the time required for the rarefaction wave to arrive). In about 10 ms it has decreased monotonically to a minimum slightly greater than the exit pressure minimum, and then increases slowly, again largely due to the transducer recovery.

We define δP to be $P_{base} - P_{exit} - P_{weight}$, where P_{weight} is the pressure due to the weight of the column (the hydrostatic head, which is typically ~1 kPa). This δP drives the fluid column up and is referred to as the thrust of the eruption [*Kanamori et al.*, 1984]. Because the thrust involves small differences between large numbers, the relative error is large. The thrust can also be estimated from the acceleration of the column (see below), which can be measured to much better precision.

Eruption Threshold

The percentage of liquid loss from the test cell is used as a measure of the magnitude of an eruption and is determined from

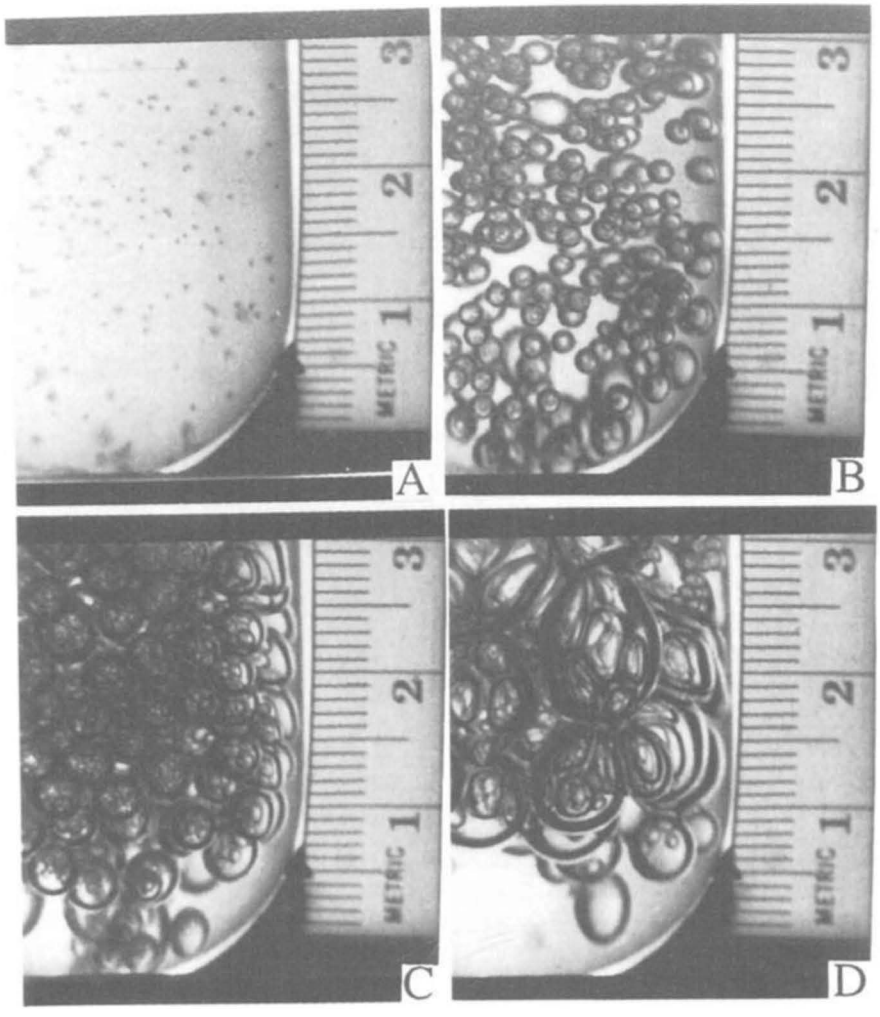

Figure 6. A sequence of photos for experiment 94 (η = 0.16 Pa s; close-up shot focusing at the base of the test cell; 4000 fps). (a) At t = 3 ms, bubbles are present and roughly randomly distributed. (b) At 30 ms, bubble sizes are greater. The diameter of most bubbles is ~1.4 mm, but there are some larger bubbles. (c) At 150 ms, the average diameter is 3.0 mm, and bubbles are still well separated. Bubbles are spherical. (d) At 340 ms, a foam is present. The lower 8 mm is almost free of bubbles. Some bubbles are merging.

the difference between the initial and the final column heights (i.e., several seconds after the eruption is over). The final liquid height measured in this way can be different from that determined from the film because some liquid drips or flows back after the eruption. When the percentage of liquid lost is plotted against P_{cell}/P_{tank} (Figure 9), there is a threshold (referred to as the eruption threshold) below which little liquid is lost (though as the threshold is approached, there may be rapid degassing/boiling) and above which a significant amount of liquid is removed from the cell. For pure CO_2-H_2O solutions at ~22 °C, the eruption threshold is at $P_{cell}/P_{tank} \approx 50$. For polymer-bearing solutions, the threshold decompression ratio decreases to ~20. The threshold may also depend weakly on P_{cell}; for example, experiments 87 and 88 have similar decompression ratio but eruption occurs only in experiment 87 in which P_{cell} is high. This dependence has not been examined in detail because the range of P_{cell} is small (due to the limit on the highest pressure that can be achieved safely). The length of the initial solution column has also been varied to examine whether it has an effect on the threshold. There is a small initial height effect when the viscosity is low and no effect when the viscosity is high (e.g., the initial height of solution in run 85 is small but there is still an eruption).

Motion of the Front

Front motion was measured directly from successive film frames. All the front motion data are shown in Figure 10. The initial motion of the front of the bubbly flow, measured from the position of the front in successive film frames, is remarkably simple. An earlier report [*Mader et al.*, 1994] has shown that the slope in a $\log(\Delta h)$ versus $\log(t - t_0)$ plot for all our experiments is close to 2, where Δh is the distance the front has traveled (height of the front minus the initial height) and t_0 is the "incubation" time or the initiation time (see equation (1) below and the caption of Figure 3). The "incubation" time is the time interval between the rupture of the diaphragm and the beginning of front motion and can be interpreted as the time for bubble nucleation. A slope of 2 in the log-log plot means that the acceleration of the motion is constant.

We examined this result further by fitting experimental data with $\Delta h = b_0(t - t_1)^n$, where b_0, n, and t_1 are fitting parameters.

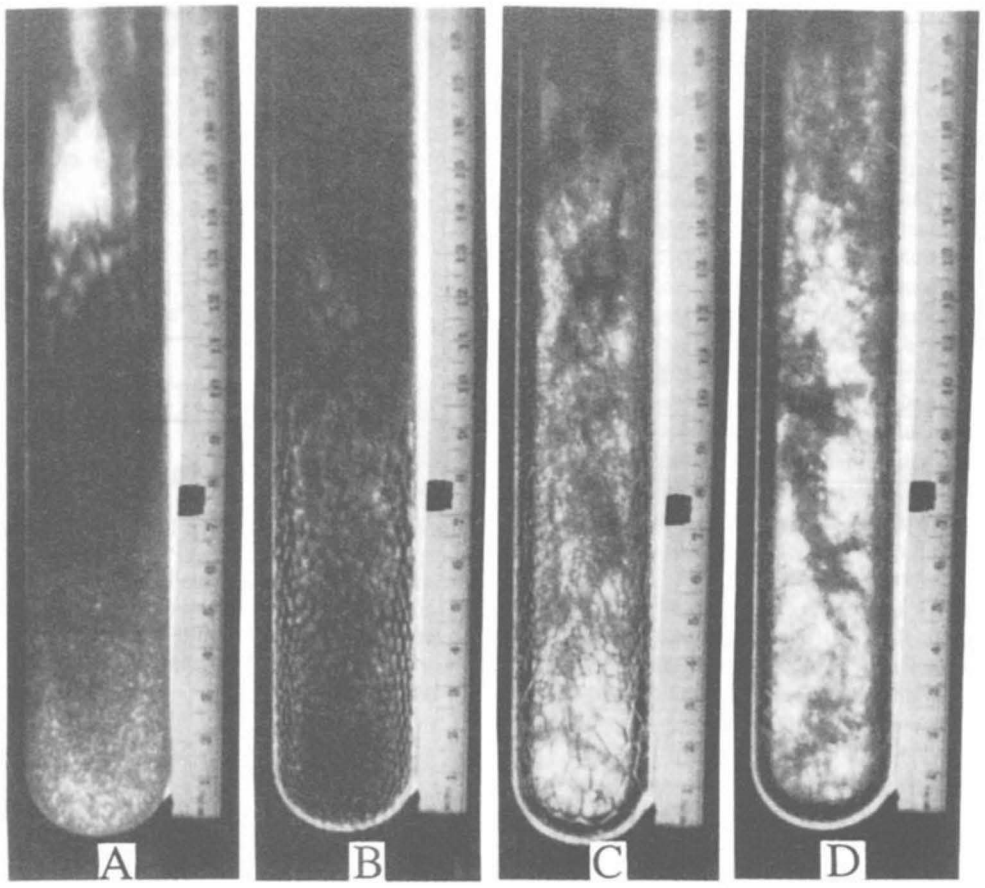

Figure 7. A sequence of photos for experiment 86 (η = 0.018 Pa s; 3000 fps; $h_{f,0}$ = 81.5 mm; the tank pressure is lower than the vapor pressure of water). (a) At 9 ms, the front reaches 130 mm. The upper 60 mm of the column is finely fragmented, and the lower 60 mm of the column is still a bubbly flow (the middle 10 mm layer is a transition zone). After another 30 ms, the column darkened due to the high number density of bubbles. (b) At 150 ms, the upper 110 mm is dark, and the lower 60 mm is a bubbly flow with large bubbles. (c) At 210 ms, there is no longer a stable bubbly flow. All the liquid films separating the bubbles vaporized because ambient pressure is lower than the vapor pressure of water. (d) At 270 ms, liquid is almost completely vaporized.

The values of n are listed in Table 5. In about 60% of the cases, n is within 10% of 2. In the other cases, n varies more (Table 5), but the average is again about 2. These results demonstrate that on average the acceleration is constant. Our result of constant acceleration differs significantly from the constant velocity (zero acceleration) of the evaporation wave generated by depressurizing a one-component liquid [*Hill and Sturtevant*, 1990].

We therefore fit all our front motion data to (Figure 10):

$$\Delta h = \frac{1}{2} a_f (t - t_0)^2, \quad (1)$$

where a_f is the acceleration of the front. Both a_f and t_0 are adjusted to achieve the best fit. The excellent fits (with R^2 values range from 0.9927 to 0.9995, where R is the correlation coefficient) in Figure 10 again demonstrate the constancy of the acceleration, one of the most important and robust results from this study. All values of acceleration and incubation time are listed in Table 5. The front acceleration ranges from 1.6 m/s^2 to ~2000 m/s^2 (0.16 to 200 g). The incubation time ranges from 0 to 7 ms except for experiments 92 and 93.

Clearly, the constant acceleration in our experiments does not continue indefinitely. If the test cell were infinitely long and there were no fragmentation, the velocity of the front would be expected to increase, then reach a maximum, and then decrease. At times later than reported in this paper, the velocity of the front may become roughly constant for a period of time [*Howard*, 1996]. The motion of the front that we observe is in the earliest phase of the eruption.

The reproducibility of the experiments was examined by comparing the results of experiments 143-152 for which the initial conditions were similar (Table 4). All of the experiments behaved similarly in that all produced eruptions. The acceleration of the front was determined for experiments 149, 150, and 152 and found to differ by a factor of ≤1.8 (Table 5). The imperfect reproducibility could reflect the random nature of nucleation and/or variations in the initial CO_2 content of the solution (see experimental procedures).

Eruption Thrust

The eruption thrust (the pressure difference between the bottom and the front of the bubbly flow) driving the bubbly flow

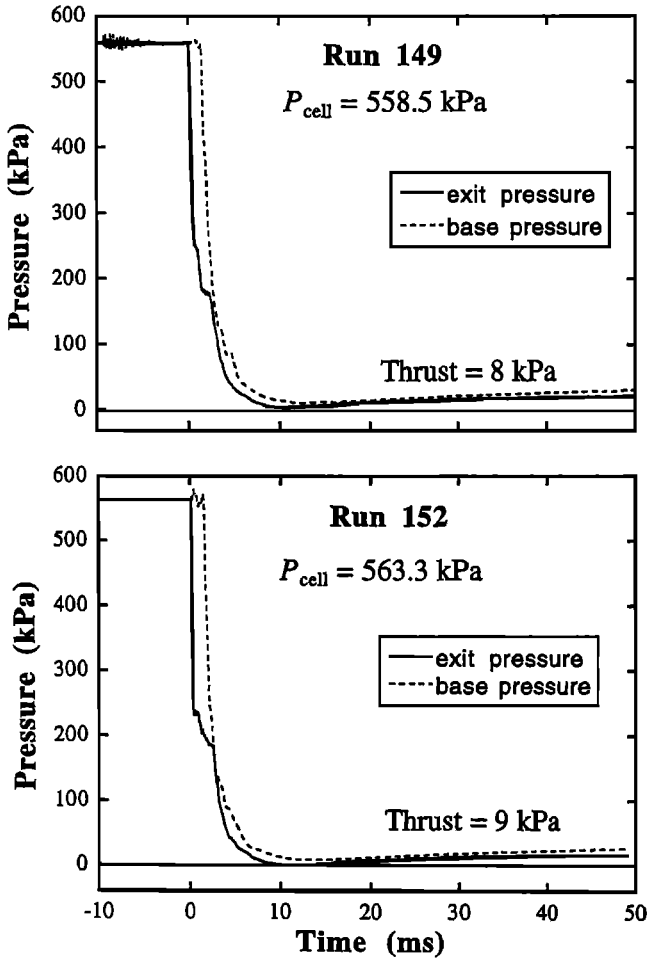

Figure 8. Exit and base pressure traces for experiments 149 and #152.

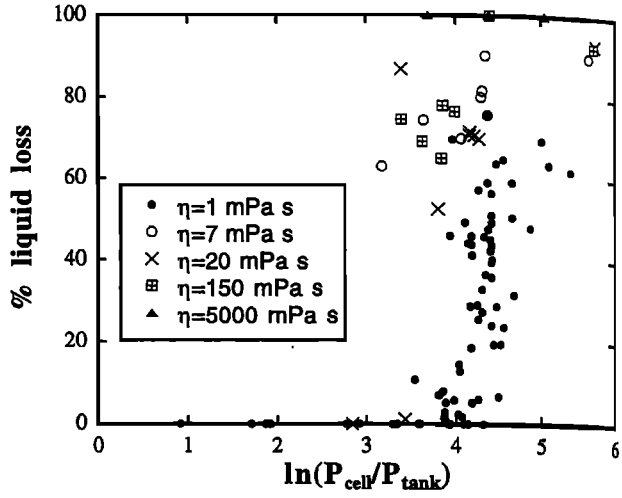

Figure 9. The percentage of liquid ejected from the test cell in an experiment versus $\ln(P_{cell}/P_{tank})$. Owing to the dripping back of water, the exact percentage is not always well-defined. There is a transition, referred to as the eruption threshold, from zero percent liquid loss to a finite amount of liquid loss. Adding polymer to the solution (increasing the viscosity of the solution) reduces the threshold.

can be calculated from the acceleration of the front and compared with the measured thrust from the base and exit pressure difference (Figure 8). Let $z = 0$ at the bottom of the bubbly flow. The thrust can be found by

$$\delta P = \int_0^{h_f} \rho a_z dz, \tag{2}$$

where h_f is the expanded column height at a given time, ρ is the density of the bubbly column ($=\rho_l h_{f,0}/h_f$, where ρ_l is the density of the liquid and $h_{f,0}$ is the initial front height), and a_z is the acceleration of fluid at height z. Assuming the flow is uniform (bubbles are uniformly distributed), a_z can be expressed as $a_z = a_f z/h_f$. Integration of equation (2) gives

$$\delta P = \frac{1}{2}\rho_l h_{f,0} a_f. \tag{3}$$

The values of the calculated eruption thrust using equation (3) for our experiments range from 0.07 kPa (experiment 92) to 95 kPa (experiment 72). The eruption thrust is roughly correlated to P_{cell}. Figure 8 shows thrusts for experiments 149 and 152 to be 8 and 9 kPa based on measured exit and base pressures, compared to the calculated 8 and 4 kPa based on the measured acceleration.

Bubble Growth

The growth of bubbles is the driving mechanism for the explosive eruption in our experiments and in natural gas-driven eruptions. For cylindrical test cells, the ascent of the front of the bubbly flow can be written as

$$\Delta h = \frac{\Delta V}{A} = \frac{4}{3A} N V_0 \pi \overline{r_b^3} = (\frac{4}{3}\pi \overline{r_b^3} N) h_0, \tag{4}$$

where ΔV is the volume increase of the whole column, A is the cross-section area of the cylindrical test cell and is constant, N is the number density of bubbles per unit liquid volume, and $\overline{r_b^3}$ is the average cube of bubble radius that depends on time. In this section we examine bubble growth in our experiments and connect it to the observed acceleration of the front of the flow.

Bubble growth was directly measured from successive film frames. The lens effect of the test cell wall was ignored in determining the size of the bubbles. Most bubbles grow smoothly, and it is the behavior of these typical bubbles that we emphasize. However, although the effect is small and will be ignored, bubble size increases slightly from the bottom to the top of the column at a given time. There are also some rare bubbles that are much bigger or smaller than average bubbles. The large ones are usually preexisting bubbles at the beginning of the experiment, or bubbles nucleated on the cell walls. The best data on bubble growth as a function of time are for polymer-bearing solutions because bubbles maintain their individuality and a roughly spherical shape to a larger size.

Figures 11a and 11b illustrate the growth of bubbles in our experiments before they begin to interact with other bubbles (i.e., before the diffusion profile or velocity field outside one bubble interferes with that of another). Although most bubbles are of similar size (bubbles 1-5 for experiment 89 and bubbles 1, 2, 3, and 6 for experiment 94), growth data for rare bubbles of significantly different size are also shown (bubbles 6 and 7 for experiment 89 and bubble 5 for experiment 94). The time dependence of bubble diameter was initially fitted with $d = d_1 t^m$, where d is bubble diameter and d_1 and m are two constants. The exponent m for 14 fits was found to range from 0.55 to 0.76, with an average of 0.674 ($\approx 2/3$), and a 2σ error on the average of 0.038. Therefore the radius of a given bubble depends on time as

$t^{2/3}$. To confirm this, some fits are shown in Figure 11 assuming that d is proportional $t^{2/3}$. The high quality of these fits supports that bubbles grow as $t^{2/3}$, i.e., significantly more rapidly than the expected $t^{1/2}$ purely diffusive growth of a single bubble in an infinite fluid [e.g., *Epstein and Plesset*, 1950]. Strong evidence for $t^{2/3}$ growth also comes from data on front ascent and bubble nucleation (see below).

The increase of bubble size in later stages where bubbles interfere with one another has also been examined. Figure 11c shows average bubble size in experiment 89 well into the foam stage (i.e., when bubbles are polyhedral). Again, best fits are obtained by assuming d is proportional to $t^{2/3}$ rather than to $t^{1/2}$.

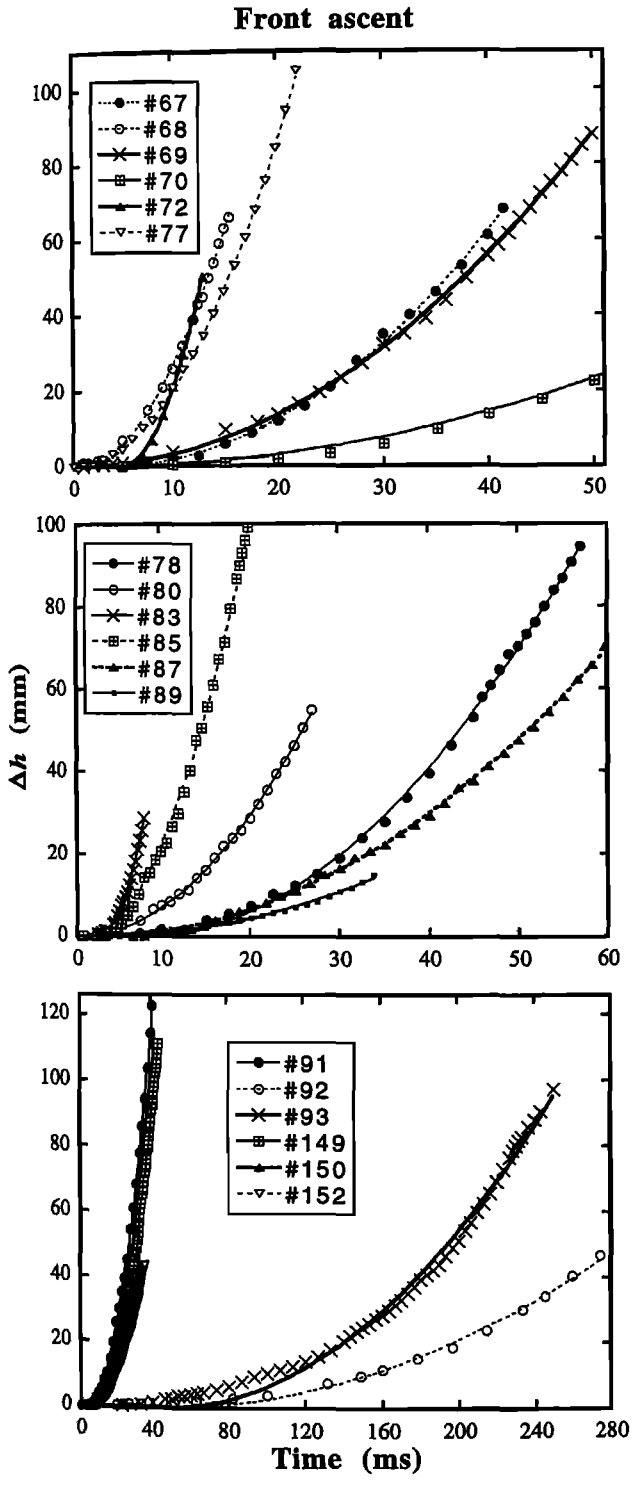

Figure 10. The distance traveled by the front (Δh) versus the time (t) after the initiation of the experiment. The data are fit by $\Delta h = 0.5a_f(t - t_0)^{1/2}$. The values of a_f (acceleration) and t_0 obtained from the fits are listed in Table 5. Some data points are outside the scale of the figure for experiments 70 and 85 so that data of other experiments can be better seen. Correlation coefficients for all fits are greater than 0.996. Though the curves for experiments 91, 149, 150, and 152 appear identical within error (due to the compressed scale), a_f values for them vary by a factor of 1.8. There are three sources of measurement error that affect the accuracy of the measured front height. One is the resolution of the picture that depends on the size of the field of view (given in Table 4). The resolution is roughly 1/300 of the field of view. The second is the blurring of a boundary (such as the front, or the bubble boundary) in the image, especially for close-up shots. The third is the shape of the front. As it rises, the front is often no longer a flat surface but a convex-up or an irregular surface. Even though effort was made to measure the "average" front position, the measurement error depends on how flat the surface is. Very often this factor dominates the measurement error. Error bars are smaller than or about the same as the size of the symbol in all cases.

Bubble Nucleation

When the decompression ratio is significantly smaller than the eruption threshold, the number density of bubbles is low. Under these circumstances, bubbles form successively from non-uniformly distributed, fixed nucleation sites (often on the test cell wall), presumably by heterogeneous nucleation. In contrast, when the eruption threshold is exceeded, all bubbles appear roughly simultaneously and are distributed roughly uniformly throughout the solution. From an examination of close-up images of such experiments in which individual and well-separated bubbles can be seen (experiments 89, 90, and 94), the nucleation of bubbles is inferred to be largely a one-time event lasting several milliseconds. Few bubbles appear before or after this nucleation event so the number density of bubbles is roughly constant in an experiment. Furthermore, in a given experiment at a given time, most bubbles are of similar size whenever bubbles are visible, which is also consistent with nucleation being a one-time event. This behavior is the same as observed in rapid cavitation by underwater explosion [*Kedrinskii*, 1985]. Combining equations (1) and (4) with the fact N is roughly constant, bubbles grow as $t^{2/3}$, consistent with the direct measurements of bubble size described above.

The number density of bubbles (N) is obtained from the close-up shots by directly counting bubbles in a given volume (experiment 94) or by dividing the total volume increase (ΔV) of the whole column by the product of V_0 and the average volume of a bubble at a given time. In the latter method, we assume that all bubbles nucleated simultaneously and are identical in size at any given time; the total volume increase is obtained by the height increase (Δh) times the cross-sectional area of the test cell, and the average bubble diameter is obtained by direct measurement of bubble size as a function of time. Estimated values of N are averages from several time steps. The number density of bubbles is ~10^7/m^3 for experiment 94 (P_{tank} was not measured), ~10^8/m^3 for experiment 89 ($P_{cell}/P_{tank} = 45$), and ~10^9/m^3 for experiment 90 ($P_{cell}/P_{tank} = 73$), suggesting a dependence of nucleation density on the degree of supersaturation. (The dependence of number density of bubbles on viscosity has not been examined.)

Table 5. Experimental Results

Experiment	Final liquid remaining, %	Total Δh, mm	n	a_f, m/s^2	t_0, ms	N, m^{-3}	a_i/h_i, s^{-2}	a_f/h_f, s^{-2}
67	64	68	1.8±0.2	93±4	3.5			
68	35	66	2.1±0.1	590±28	0.5			
69	71	88	2.03±0.03	72±2	0.4			
70	95	87	1.6±0.1	20.4±0.4	2.3			
71	0	49		too low ambient pressure				
72	19	50	1.6±0.1	1528±130	4.8			
77	29	105	2.07±0.03	444±10	0.5			
78	9	94	2.4±0.2	75.5±2.8	7.0			
80	5	55	2.03±0.04	152±5	0.3			
83	49	29	2.6±0.4	1850±85	2.6			
84	94		front not well-defined due to fragmentation					
85	29	155	1.7±0.1	524±13	1.8			
86	0	73		too low ambient pressure				
87	13	70	2.0±0.1	40.9±0.8	1.7			
88	99			no eruption				
89	48	15	2.2±0.1	28.0±2.6	1.9	~10^8	244±125	333±30
90	0		too many initial bubbles at the front			~10^9		
91	30	123	2.0±0.1	170±4	3.2			
92	26	47	2.5±0.1	1.64±0.18	40			
93	31	97	2.7±0.1	4.6±0.4	46			
94	7			front is not in the view		~10^7		
143	56			front is not in the view				
145	76			front is not in the view				
147	61			front is not in the view				
148	64			front is not in the view				
149	58	111	2.1±0.1	155±2	5.9			
150	51	35	2.1±0.1	132±3	5.2		13.1±2.0	12.8±0.3
152	57	44	2.0±0.1	85.2±1.2	3.8			

Final liquid that remains in the test cell is measured after the experiment (not based on film) and may hence be slightly different from films due to the dripping back of liquid. Total Δh is total front motion measured in each experiment. The front height measurement ends when the front moves out of the field of view. n is btained by fitting $\Delta h = b_0(t-t_1)^n$. When t_1 is less than zero from the fit, t_1 is assumed to be zero and the data are refit to obtain n. Errors are the fitting errors (with equal weight to each Δh value though we know some Δh values have greater uncertainty) given at the 2σ level. The value of n gives an objective assessment as to whether the acceleration is constant. a_f (acceleration of the front) and t_0 (incubation time) are obtained by fitting $\Delta h = 0.5a_f(t - t_0)^2$. N is number density of bubbles (per unit liquid volume). a_i is acceleration of layer i (that is initially at height h_i).

These bubble nucleation densities are similar to those in crystal-free rhyolitic melts with a supersaturation of 15-20 MPa reported by *Hurwitz and Navon* [1994] but much lower than those they reported in crystal-bearing melts.

Bubble Ascent

Bubble ascent data are obtained by measuring the center position of bubbles from successive film frames in close-up images. Although we tried to avoid bubbles on the test cell wall, the bubbles whose ascent has been measured are probably nevertheless close to the wall. Because bubbles near the wall ascend slower due to friction with the wall, the measurement may thus yield lower ascent rates than bubbles nearer the center axis of the test cell.

Figure 12 shows data on bubble ascent. There are two components to the ascent of bubbles in the erupting column: the first (the "expansion ascent") is due to growth of bubbles below the layer under consideration, which leads to volume expansion of the whole column of bubbly flow; the second is buoyant rise of the bubbles relative to the surrounding liquid. The role of buoyant rise of bubbles in their overall ascent (which also includes the effect of the expansion of bubbles in the column) has been evaluated as follows. We compared the ascent of individual bubbles with calculated buoyant rise using published values of drag versus Reynolds number for a rigid sphere in an infinite fluid [*Clift et al.*, 1978]. The applicability of such a calculation has been confirmed by others [e.g., *Shafer and Zare*, 1991] and by our own direct measurement (data not shown). The comparisons are shown in Figure 12. In higher-viscosity experiments with an eruption, the buoyant rise of bubbles is less important than the expansion ascent. In experiments on the less viscous solutions in which little or no eruption occurs, buoyant rise can be seen on the order of several hundreds of milliseconds after rupture of the diaphragm. Based on Figure 12, we confirm that the importance of buoyant rise decreases with viscosity and is not a major factor compared to the overall ascent at high viscosities (≥0.1 Pa s). For example, for experiment 89, as the front leaves the view at 34 ms, the buoyant rise velocity of bubbles is 0.17 m/s, whereas the velocity of the front is 0.95 m/s. Our experiments at high viscosity match natural eruptions of silicic magmas in this key respect because buoyant rise of bubbles during an explosive eruption is not important given the high viscosities of rhyolitic magmas (note that at low Reynolds number the velocity of buoyant rise is inversely proportional to viscosity).

As illustrated in Figure 12 for selected experiments, the overall ascent of bubbles can be approximated by a constant acceleration, in agreement with our conclusion based on the motion of the front. Furthermore, for experiments 89 and 150, for which both bubble ascent and front ascent data are available, a_i/h_i (where subscript i means layer i) values for all bubbles are in reasonable agreement with a_0/h_0 obtained from measured front ascent: for experiment 89, the average a_i/h_i based on ascent of seven bubbles is 244±125 s^{-2} versus a value of 333±30 s^{-2} based on the front motion; for experiment 150, a_i/h_i based on the ascent of a single bubble is 13.1±2.0 s^{-2} versus a value of 12.8±0.3 s^{-2} based on front ascent. This confirmation of the constancy of the acceleration and of its actual value from two different measurements gives us added confidence in the robustness of this result.

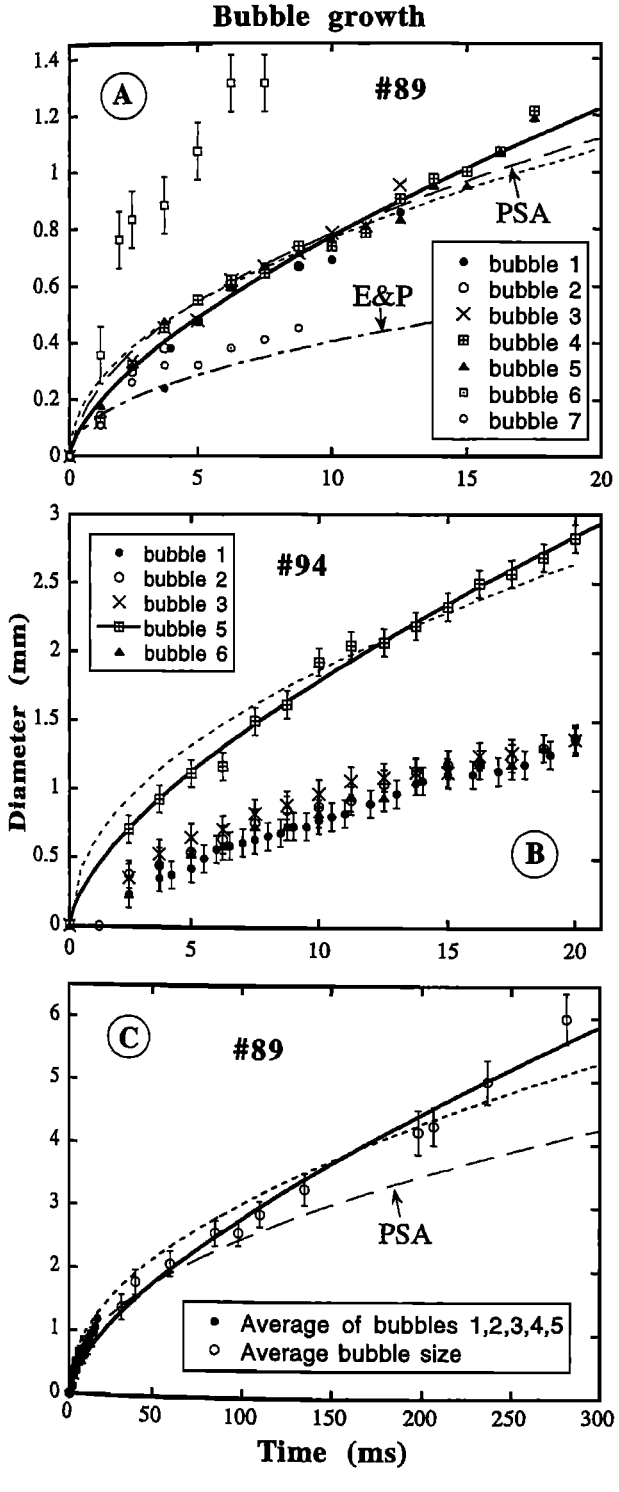

Figure 11. Bubble growth in experiments 89 and 94. (a) The diameter (d) of individual bubbles in experiment 89 is plotted against time. The 2σ error in d is ~0.1 mm, and for clarity, the error bars for most data are not shown. Shown are best fit curves assuming d is proportional to $t^{1/2}$ (short dashes) and $t^{2/3}$ (solid curve) for bubbles 1-5 (all five bubbles are fit by a single curve). The curve marked as E&P is calculated using the approach of *Epstein and Plesset* [1950]. The curve marked as PSA is calculated using the program of *Proussevitch et al.* [1993a]. (b) d versus t in experiment 94. Best fit curves assuming d is proportional to $t^{1/2}$ (short dashes) and $t^{2/3}$ (solid curve) for bubble 5 are shown. The tank pressure for experiment 94 was not recorded before the experiment so bubble growth could not be forward-modeled using the program of *Proussevitch et al.* [1993a]. (c) The growth of average bubbles in experiment 89. Individual bubbles are not tracked; only the average size of bubbles is estimated. Best fit curves assuming d is proportional to $t^{1/2}$ (short dashes) and $t^{2/3}$ (solid curve) are shown. Average bubble diameter at 280 ms may be significantly affected by coalescence. For comparison, the average diameter of bubbles 1-5 shown in Figure 11a is also shown. The curve marked as PSA is calculated using the program of *Proussevitch et al.* [1993a].

Foam Stability and Fragmentation

The vesicularity limit of a foam is important in the dynamics of eruptions [*Fink*, 1995]. In the CO_2-H_2O system, fragmentation occurs roughly at 70-80% vesicularity and no stable foam develops. When a polymer is added to the solution (i.e., increasing the viscosity), high vesicularity foam becomes stabilized and fragmentation is suppressed. The vesicularity of the flow can be estimated using $(V\text{-}V_0)/V$ if the total volume V of the bubbly flow is known. However, because the total volume of the column cannot be observed after the column front moves out of the test cell and into the tank, we estimated the vesicularity of the foam from close-up shots from which both the number density and sizes of bubbles could be determined.

For experiment 89 (viscosity is 0.018 Pa s, P_{cell} = 496 kPa, P_{tank} = 11 kPa), the number density of bubbles was ~1 per 10 mm^3 liquid volume. When the dominant bubble diameter reached ~4 mm (at 150 ms), the vesicularity was ~77% ($4\pi r_b^3/3/[10+4\pi r_b^3/3]$) and a foam formed (i.e., it can be seen that bubbles were touching and changing from spherical to polyhedral shape). The vesicularity of this foam is consistent with *Cashman and Mangan*'s [1994] definition of foam as having a vesicularity greater than 74%. At the end of the film, only a few bubbles had merged because the motions had been so gentle ($a_i \approx 0.2g$ for the layer in the field of view) and the foam was still stable. At this time (360 ms), the polyhedral bubbles had an average "diameter" >6 mm, and the vesicularity of the foam was calculated to be ~92%. The average thickness of the liquid film separating the bubbles (ignoring the presence of plateau borders) is calculated to be ~170 μm.

For experiment 90 (viscosity is 0.005 Pa s, P_{cell} = 524 kPa, P_{tank} = 7.2 kPa), the number density of bubbles was ~1 per 0.9 mm^3 liquid volume. When bubble diameter reached ~2 mm with a calculated vesicularity of 82% (~75 ms), a visible foam already formed. When polygonal bubble "diameter" exceeded 3 mm at

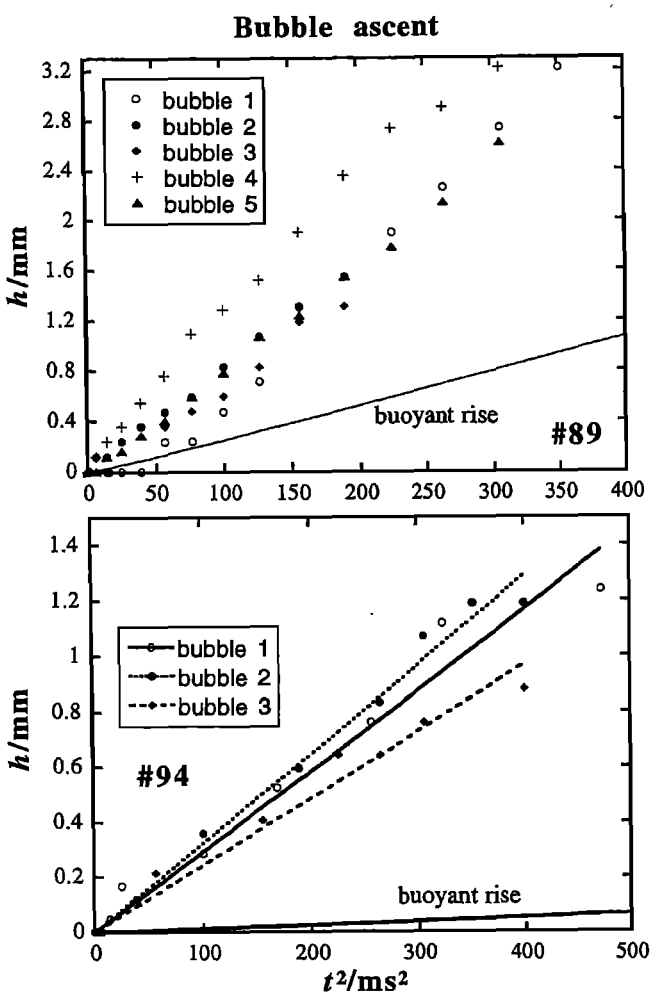

Figure 12. Measured overall bubble ascent plotted against time in experiments 89 and 94. For experiment 94, the data are fit by $\Delta h_i = 0.5 a_i t^2$, shown as lines. Measurement error (2σ) on Δh_i is about 0.15 mm. Calculated buoyant rise is also shown. In calculating buoyant rise, the acceleration due to gravity (g) is replaced by $g + a_i$ (where a_i is the upward acceleration of the layer to which the bubble belongs) to account for motion in an accelerating reference frame.

~135 ms (a vesicularity exceeding 93%), some bubbles merged but the foam did not fragment.

In experiment 85 (viscosity is 0.018 Pa s, P_{cell} = 618 kPa, P_{tank} = 10 kPa), the vesicularity as the erupting front moves out of the field of view is calculated from $\Delta h/(\Delta h + h_0)$ as 82%. At this time (26 ms), average bubble diameter is <2 mm, corresponding to a number density of bubbles of >1 per mm^3 of liquid volume. At the end of film (746 ms) near the bottom of the flow where accelerations had been less than 8 g, the average bubble "diameter" in the stable foam is about 4 mm, corresponding to a vesicularity of >97%, and the average thickness of liquid separating the bubbles is calculated to be ~40 μm.

The key result of the polymer-bearing experiments is that bubbles in this polymer-water system do not cease growth at gas/liquid volume ratios of 3:1 to 5:1 and foams can be stable with vesicularity up to 97%, contrary to the prediction of *Sparks* [1978]. That the vesicularity is greater than that corresponding to closest packing of uniform spheres (74% vesicularity) reflects that bubble shape in these foams is polyhedral rather than spherical. Pumices and reticulites with up to 98% vesicularity have been reported [*Thomas et al.*, 1994; *Cashman and Mangan*, 1994], and in this respect, our experimental results are comparable with the eruption products of basaltic and silicic magmas.

There are two different styles of fragmentation in our experiments. The first is fragmentation at the flow front (the surface of the flow). This occurs to some extent in all experiments in which eruption occurs and is the process by which the initially smooth interface between the bubbly flow and the vapor above it becomes an irregular interface (e.g., Figure 4b). This process may be termed either surface fragmentation or heterogeneous fragmentation. The surface fragmentation may propagate downward more rapidly than the rise of the surface and cause the fragmentation of the whole column. The second is fragmentation throughout the accelerating column by the bursting of individual bubbles and the formation of a continuous gas phase containing droplets. This is a roughly uniform process. Only when this type of fragmentation occurs, does the foam become unstable and disintegrate in a very short time. This process may be termed either body fragmentation or homogeneous fragmentation. This second type of fragmentation is most apparent in polymer-free CO_2-H_2O experiments and polymer-bearing solutions with viscosity below 0.02 Pa s. At low viscosity, bubbles break up at relatively small size, making a foam unstable. In experiments with higher viscosities, a foam is often stable in the course of the experiment, and individual bubbles maintain their identity even when they deform into polygonal shape. Body fragmentation probably depends more on decompression rate (stress vs. strength) and viscosity than on vesicularity.

Even though fragmentation does occur in some of our experiments, explosive eruption occurs whether or not there is fragmentation. That is, explosive eruptions are not due to fragmentation, but due to volume expansion caused by bubble growth. Fragmentation does not necessarily occur at 74% vesicularity because bubbles are not necessarily spherical.

Discussion

Homogeneous or Heterogeneous Bubble Nucleation?

During our experiments, bubbles appear uniformly throughout the solution. Although this is consistent with homogeneous nucleation, two lines of evidence suggest that the nucleation is more likely to have been heterogeneous on microscopic nuclei in the liquid. One is that classical nucleation theory predicts that there should be negligible homogeneous nucleation due to the relatively small pressure differences (ΔP < 0.8 MPa) involved in our experiments [*Sparks*, 1978]. The other is that nucleation in our experiments appears to be an essentially one-time event lasting only several milliseconds. In the first 20 ms or so, a large amount of the solution is far enough away from small bubbles that new bubbles would be expected to have nucleated there, spreading the nucleation event over a longer time interval, if homogeneous nucleation dominated. We therefore infer that the nucleation occurred predominantly on preexisting nucleation sites roughly uniformly distributed in the solution, consistent with the conclusion of *Hurwitz and Navon* [1994] on nucleation in crystal-free rhyolitic melts.

Bubble Growth

We have shown that bubbles grow as $t^{2/3}$ (instead of $t^{1/2}$) in our experiments based directly on measurements of bubble size and indirectly on measurements of front ascent as a function of time. (Note that in our experiments, expansion growth due to progressively decreasing pressure is negligible because the ambient pressure is roughly constant during bubble growth.) The observed $t^{2/3}$ growth is significantly more rapid than the $t^{1/2}$ dependence predicted for diffusive growth of a spherical bubble in an infinite fluid medium in which convection and surface tension are negligible [*Epstein and Plesset*, 1950]. This is shown clearly in Figure 11a, which compares our data with bubble growth predicted by *Epstein and Plesset* [1950] assuming CO_2 diffusivity in the high-viscosity solution to be the same as that in dilute CO_2 solution (i.e., ignoring the possible effect of decreasing diffusivity by increasing viscosity). The calculated bubble growth is roughly half the observed growth in experiment 89 in the first 15 ms. If D is assumed to be inversely proportional to η, the calculated growth would be only 1/8 of the observed growth.

Proussevitch et al. [1993] modeled diffusive bubble growth due to sudden decompression to a constant pressure, including the effects of boundary motion, film thinning due to boundary expansion, finite fluid volume, surface tension, and viscosity. The only difference between their model and our experiments is that bubble buoyant rise and other forms of advection may play some role in our experiments. We obtained a copy of their program and modified the functional dependence of solubility on the partial pressure of the volatile component to match that of CO_2 in water. Curves marked as PSA in Figures 11a and 11c show the results of their model (also assuming D does not decrease by increasing viscosity); note that these curves are not fits to the data, but forward models based on measured properties of CO_2-H_2O solutions. The modeled bubble growth agrees with our data well at small times (Figure 11a), but differs slightly but systematically at greater times (Figure 11c). This reflects the fact that even with the inclusion by *Proussevitch et al.* [1993] of additional factors influencing bubble growth, the modeled bubble growth is closer to $t^{1/2}$ growth than the observed $t^{2/3}$ growth.

We know of three published models in which a $t^{2/3}$ dependence of bubble growth is predicted. (1) *Toramaru* [1989] carried out numerical calculations and concluded that under the condition of a constant decompression rate and no interaction among bubbles, bubbles grow as $t^{2/3}$. The model results do not apply to our work because in our experiments pressure is reduced suddenly and bubble growth occurs in a constant ambient pressure instead of constant decompression rate. (2) *Sparks et al.* [1994] predicted $t^{2/3}$ growth for elongated bubbles stretched at a constant rate. The results again do not apply to our work because in our experiments, bubble shapes evolve from spherical, to oblate, then to spherical, and then to polyhedral (see earlier discussions), instead of being stretched to prolate at a constant rate. (3) *Levich* [1962] showed that the boundary layer thickness (δ) is $(3\pi/2)^{1/2}(Dr_b/U)^{1/2}$ for small Reynolds numbers [*Levich*, 1962, equation 91.5, p. 467] and $(\pi/2)^{1/2}(Dr_b/U)^{1/2}$ for moderate Reynolds numbers [*Levich*, 1962, equation 91.8, p. 468], where U is the velocity of buoyant rise of a bubble in the liquid. If both U and ρ_b are constant, a bubble grows as $t^{2/3}$ [*van Wijngaarden*, 1967]. For example, for moderate Reynolds numbers, combining

$$\frac{dr_b}{dt} = q\frac{D}{\delta}, \tag{5}$$

where $q = (C_0 - C_s)/\rho_b$, and the above expression for δ, then,

$$r_b = (\frac{9}{2\pi} UDq^2)^{1/3} t^{2/3}. \tag{6}$$

Although the buoyant rise velocity is not expected to be constant for a single small undeformed bubble in an infinite fluid as it grows, for eruption experiments in which many bubbles interact, it may be possible that the buoyant rise reaches a constant terminal velocity at a small bubble size. Although experiments specifically designed to test it are required, buoyant rise of bubbles (though insignificant compared to expansion ascent), as developed by *Levich* [1962] and *van Wijngaarden* [1967], may play an important role in the $t^{2/3}$ bubble growth in our eruption experiments. Advection that leads to roughly spherical bubble shape in a stretching flow may also play a role in the $t^{2/3}$ growth of bubbles.

In the context of the above explanation, whether or not the $t^{2/3}$ growth observed in our experiments is applicable to natural eruptions, even under the same hypothetical instantaneous decompression, seems to depend on the viscosity since viscosity controls the velocity of buoyant rise of bubbles. However, the experiments by Phillips et al. (personal communication, 1996) using the acetone and gum rosin system (viscosity is ~10^6 Pa s) also showed constant acceleration, implying that bubbles probably grow as $t^{2/3}$. Hence $t^{2/3}$ growth of bubbles and constant acceleration may be common for eruptions after sudden decompression, even though the cause of such growth may be different. In natural eruptions, pressure on each layer of bubbly magma decreases as the layer ascends. Hence bubble growth rate will be different (see later discussion).

Comparison With Chemical Mixing Experiments

Mader et al. [1994] reported both our experimental approach and the other approach more fully described by *Mader et al.* [1996]. Our approach is different from that of *Mader et al.* [1996] in that they mix acid and a carbonate solution to generate supersaturation in CO_2, whereas we first fill the test cell with solution that is roughly uniformly saturated with CO_2 at a high pressure and then depressurize the test cell to generate supersaturation in CO_2. *Mader et al.* [1996] have generated greater supersaturations than we have, but their results are more difficult to quantify due to mixing and chemical reaction. Their approach best simulates eruption caused by mixing of different magmas or mixing between magma and water, while ours simulates gas-driven lake and volcanic eruptions of a roughly uniformly supersaturated liquid.

Limnic Eruptions

Most authors now agree that the massive CO_2 gas releases from Lakes Nyos and Monoun were due to the release of initially dissolved CO_2 in the lake water during a lake overturn or a limnic eruption [*Freeth and Kay*, 1987; *Kling et al.*, 1987; *Freeth et al.*, 1990; *Sabroux et al.*, 1990]. However, *Tazieff* [1989], assuming that lake overturns and limnic eruptions would not be violent, suggested that the eruption was volcanic. Our experimental results show that CO_2 dissolved in water can power violent eruptions. One way in which CO_2 release from a lake overlying a magmatic zone could occur is as follows [*Zhang*, 1996, and references therein]: Owing to gradual CO_2 leakage from the underlying magma into the bottom water of the lake, the CO_2 concentration increases with water depth. Direct measurements show that saturation of bottom water at Lakes Nyos and Monoun

could be reached on a timescale of decades [*Kling et al.*, 1994]. The CO_2-rich deep water is denser than CO_2-poor water, leading to stably stratified lake. However, the system can become unstable if a perturbation moves deep water to shallower levels at which it is supersaturated with respect to CO_2. Once the water is supersaturated with CO_2, bubbles form and grow in the water. Being less dense than the surrounding water, the bubbly water ascends with increasing speed, resulting in a limnic eruption and the release of CO_2 into the atmosphere. Rise of CO_2-saturated water may be violent because of strong positive feedback between bubble formation and growth, volume expansion, and buoyant rise that causes reduction of ambient pressure. The exit velocity increases with the initial dissolved CO_2 content (hence with the depth of saturation). *Zhang* [1996] shows that maximum exit velocity from Lake Nyos could be as high as ~90 m/s. Because the viscosity is low, a foam is not expected to be stable, and bubbles break up and rupture at roughly 70-80% vesicularity. Hence as in our experiments, bubbly flow fragments into a gas flow carrying water droplets either inside the lake or above the surface of the lake. Larger droplets are expected to rain down near the vent and finer droplets are carried by the gas flow further away. Because CO_2-rich gas is denser than air, the erupting column collapses to form a CO_2 density flow down the flank of the lake.

It has been hypothesized that in one of the Galilean satellites, Europa, "volcanic" eruption may result from the melting of water ice, forming a "water magma" enriched in CO_2 [*Crawford and Stevenson*, 1988]. Such a "magma" could become supersaturated in CO_2 by ascent, by the crystallization of nearly CO_2-free ice, or by bubble overpressure. If the level of supersaturation exceeds the eruption threshold, an eruption similar to what we have simulated in our experiments would occur.

Applications to Gas-Driven Volcanic Eruptions

Although our experiments simulate the explosive volume expansion of a rapidly depressurized gas-saturated magma, there are important differences between our experiments and natural volcanic eruptions. For example, in natural eruptions, after the initial pressure decreases (e.g., by landslide of overlying rocks, sector collapse, or other conduit clearing mechanisms [*Wilson et al.*, 1978]), the ambient pressure decreases further as the erupting column rises; in contrast, in our experiments, the ambient pressure decreases nearly instantaneously to a constant value because the hydrostatic head is small. The gradual pressure reduction in natural eruptions means bubble growth depends even more strongly on time than for the case of constant pressure because of two effects. One is an expansion effect; i.e., as the ambient pressure decreases, bubbles expand even further. The second is a mass transfer effect; i.e., as the ambient pressure decreases, the equilibrium surface concentration of the volatile component decreases, steepening the concentration gradient. As a result, mass transfer to the bubble increases, and bubble radius increases more rapidly than in the case of constant ambient pressure. Model calculations by *Toramaru* [1989] showed that if convection and interaction between bubbles can be ignored, bubbles grow as $t^{2/3}$ under constant decompression rate (linear decompression), more rapid than diffusive bubble growth ($t^{1/2}$) under constant pressure. However, our experiments suggest that more realistic modeling should consider the interaction between bubble growth and ascent. If modeling the interaction between bubble growth and ascent is not possible, using accelerating decompression rate is more reasonable than constant decompression rate.

Besides the difference in the rate of decompression, quantitative applications of our results to natural volcanic eruptions require a model that incorporates the effects of parameters such as diffusion, viscosity, surface tension, and the solubility of the volatile component in the liquid. We are in the process of developing such a model so that our experimental results can be scaled to natural eruptions. Our experiments show that an increase of viscosity changes the dynamics of the eruption (such as foam stability) and the eruption threshold. Higher viscosity will minimize the importance of buoyant rise of bubbles. The effect of diffusivity of the gas species has not been explored experimentally but smaller diffusivity in magmatic systems than in CO_2-H_2O system would reduce bubble growth rate and hence the velocity of the bubbly flow. The shape and size of the magma chamber and the conduit may also have a significant effect on the eruption dynamics [*Wilson et al.*, 1980]. The simulated eruptions mimic the violence and elegance of natural eruptions and provide insight to help us develop quantitative models.

There was some misconception that explosive eruptions occur only when the viscosity is high. Our experiments and limnic eruptions show that low-viscosity fluids can erupt violently under the right conditions. Viscosity plays a role but not a determining role in whether there can be an explosive eruption. We suggest that explosive basaltic eruption is rare because basaltic magma typically contains less amount of volatile (H_2O + CO_2) content. With high volatile content, basaltic magma may erupt violently despite its low viscosity [*Williams*, 1983].

On the basic of experimental results discussed above and observations of pumices and reticulites [*Thomas et al.*, 1994; *Cashman and Mangan*, 1994], fragmentation does not necessarily occur at 74% vesicularity. Fragmentation probably depends more on decompression rate (stress vs. strength, [*Alidibirov and Dingwell*, 1996]) and viscosity than on vesicularity. This result is important to modeling gas-driven eruptions because the erupting flow before fragmentation is a roughly uniform bubbly flow, and after fragmentation it is a gas flow carrying liquid droplets. The velocity of a bubbly flow is controlled by the kinetics of bubble growth, whereas the velocity of a gas flow is controlled by gas dynamics.

Concluding Remarks and Future Work

We investigated one type of gas-driven eruptions through experiments. Our experiments simulate eruptions with high accelerations and velocities using a simple gas-liquid system with the gas initially uniformly dissolved in the liquid. The high-speed motion pictures illustrate the dynamics of gas-driven eruptions and provide details of the eruption process and intuitive insights into natural eruptive processes. There is a threshold level of supersaturation above which an eruption will occur and below which there will be no eruptions. The gas-driven eruption is powered by the growth of bubbles and expansion of the gas phase. Buoyant rise of bubbles is minor compared to the upward motion of bubbles due to the expansion of the system but may be significant in increasing bubble growth rate. The initial motion of the eruption column is remarkably simple, characterized by a constant acceleration if the ambient pressure is constant. Under such conditions, bubbles grow as $t^{2/3}$.

Even though they are all driven by gas exsolution from a liquid and they are all controlled by bubble growth and gas expansion, the type of gas-driven eruptions that we investigated through experiments does not match exactly natural gas-driven

eruptions in some aspects. In natural gas-driven eruptions, surrounding pressure is not constant, but decreases as the erupting column rises. Hence, the flow is likely characterized by increasing acceleration. Decompression rate likely increases with time. Limnic eruptions, unlike the simulated eruptions, is through a fluid medium and buoyancy plays a determining role. In explosive volcanic eruptions, the material properties are different from our analog system. Therefore direct quantitative application requires an understanding of these differences.

Our experiments show: (1) Eruptions powered by CO_2 exsolution from water, known to occur in lakes in so-called limnic eruptions, can be violent. (2) Explosive eruptability depends more on dissolved gas content than on melt viscosity. CO_2-melt systems may not be able to power an explosive eruption due to low CO_2 solubility. Basaltic melt containing high H_2O and water containing high CO_2 may erupt violently. (3) Although fragmentation plays an important role in the dynamics of gas-driven eruptions, explosive eruptions are not due to fragmentation, but due to volume expansion caused by bubble growth or gas expansion. Fragmentation does not necessarily occur at 74% vesicularity. Fragmentation probably depends more on decompression rate (stress versus strength [*Alidibirov and Dingwell*, 1996]) and viscosity than on vesicularity.

Future work includes developing scaling laws, perfecting the experimental technique to improve reproducibility, and examining the effects of factors such as chamber shape, viscosity, solubility, diffusivity, surface tension, etc. on the dynamics of gas-driven eruptions.

Notation

a_f upward acceleration of the front.
a_i upward acceleration of layer i or bubble i in the column.
a_z upward acceleration at height z.
A cross-section area of the cylindrical test cell.
C_0 initial concentration of CO_2 in the solution.
C_s saturation concentration of CO_2 at the liquid interface with bubbles.
d diameter of a bubble.
D diffusivity of CO_2 in water.
g downward acceleration due to gravity.
h_f height of the front of the gas-liquid column at any time.
$h_{f,0}$ initial height of the front.
h_i height of layer i at any time.
$h_{i,0}$ initial height of layer i.
N number of bubbles per unit liquid volume.
P pressure.
P_{base} pressure at the bottom of the test cell.
P_{cell} pressure in the test cell before decompression.
P_{exit} pressure at the exit (from the test cell to the tank)
P_{tank} pressure in the tank before decompression.
P_{weight} pressure due to the weight of the overlying liquid or bubbly column.
q dimensionless parameter; $q=(C_0 - C_s)/\rho_b$, where C and ρ_b have the same unit.
r_b radius of a bubble.
R gas constant.
t time.
t_0 incubation time.
T temperature.
U velocity of buoyant rise of a bubble.
v_f velocity of the front.
v_i velocity of layer i.
V volume of the whole bubble+liquid column.
V_0 initial volume of the liquid.
z the vertical coordinate.

δ thickness of the boundary layer through which mass must be transported to the bubble.
Δh distance traveled by the front ($\equiv h_f - h_{f,0}$).
ΔP difference between required saturation pressure and ambient pressure, equal to $P_{cell} - P_{tank}$.
δP eruption thrust, equal to $P_{base} - P_{exit} - P_{weight}$.
η viscosity.
ρ density.
ρ_b: density of gas in bubbles.
ρ_l: density of liquid.

Acknowledgments. D. Pyle was initially involved in this project, and we thank him for his contribution. We thank A. Proussevitch and D.L. Sahagian for making the bubble growth program available and K.V. Cashman, W. Nash, and K. Wohletz for insightful and constructive comments. Y.Z. thanks X. Feng for numerous discussions and help. This research is partially supported by NSF grants EAR-9304161 and EAR-9458368 and DOE grant DE-FG03-85ER1344.

References

Alidibirov, M., and D.B. Dingwell, Magma fragmentation by rapid decomposition, *Nature*, *380*, 146-148, 1996.

Bagdassarov, N.S., and D.B. Dingwell, Frequency dependent rheology of vesicular rhyolite, *J. Geophys. Res.*, *98*, 6477-6487, 1993.

Cashman, K.V., and M.T. Mangan, Physical aspects of magmatic degassing II. Constraints on vesiculation process from textural studies of eruptive products, *Rev. Mineral.*, *30*, 447-478, 1994.

Clift, R., J.R. Grace, and M.E. Weber, *Bubbles, Drops, and Particles*, 380 pp., Academic, San Diego, Calif., 1978.

Crawford, G.D., and D.J. Stevenson, Gas-driven water volcanism and the resurfacing of Europa, *Icarus*, *73*, 66-79, 1988.

Cussler, E.L., *Diffusion: Mass Transfer in Fluid Systems*, 525 pp., Cambridge Univ. Press, New York, 1984.

Dean, J.A., Lange's Handbook of Chemistry, 1856 pp., McGraw-Hill, New York, 1985.

Epstein, P.S., and M.S. Plesset, On the stability of gas bubbles in liquid-gas solutions, *J. Chem. Phys.*, *18*, 1505-1509, 1950.

Fink, J., Exploding volcanic myths, *Nature*, *373*, 660-661, 1995.

Freeth, S.J., and R.L.F. Kay, The Lake Nyos gas disaster, *Nature*, *325*, 104-105, 1987.

Freeth, S.J., G.W. Kling, M. Kusakabe, J. Maley, F.M. Tchoua, and K. Tietze, Conclusions from Lake Nyos disaster, *Nature*, *348*, 201, 1990.

Frohlich, G., Interaction experiments between water and hot melts in entrapment and stratification configurations, *Chem. Geol.*, *62*, 137-147, 1987.

Hill, L.G., and B. Sturtevant, An experimental study of evaporation waves in a superheated liquid, in *Adiabatic Waves in Liquid-vapor Systems*, edited by G.E.A. Meier and P.A. Thompson, pp. 25-37, Springer-Verlag, New York, 1990.

Howard, D.D., Exsolution of volatiles, part II, Ph.D. thesis, Calif. Inst. of Technol., Pasadena, 1996.

Hurwitz, S., and O. Navon, Bubble nucleation in rhyolitic melts: Experiments at high pressure, temperature, and water content, *Earth Planet. Sci. Lett.*, *122*, 267-280, 1994.

Jaupart, C., and S. Tait, Dynamics of eruptive phenomena, *Rev. Mineral.*, *24*, 213-238, 1990.

Jaupart, C., and S. Vergniolle, Laboratory models of Hawaiian and Strombolian eruptions, *Nature*, *331*, 58-60, 1988.

Jaupart, C., and S. Vergniolle, The generation and collapse of a foam layer at the roof of a basaltic magma chamber, *J. Fluid Mech.*, *203*, 347-380, 1989.

Kanamori, H., J.W. Given, and T. Lay, Analysis of seismic body waves excited by the Mount St. Helens eruption of May 18, 1980, *J. Geophys. Res.*, *89*, 1856-1866, 1984.

Kedrinskii, V.K., Peculiarities of bubble spectrum behavior in cavitation zone and its effect on wave field parameters, in *Ultrasonics International 85*, edited by Z. Novak, pp. 225-230, Butterworth Sci., Guildford, England, 1985.

Kieffer, S.W., Numerical models of caldera-scale volcanic eruptions on Earth, Venus, and Mars, *Science, 269*, 1385-1391, 1995.

Kieffer, S.W., and B. Sturtevant, Laboratory studies of volcanic jets, *J. Geophys. Res., 89*, 8253-8268, 1984.

Kirkpatrick, R.J., Kinetics of crystallization of igneous rocks, *Rev. Mineral., 8*, 321-398, 1981.

Kling, G.W., M.A. Clark, H.R. Compton, J.D. Devine, W.C. Evans, A.M. Humphrey, E.J. Koenigsberg, J.P. Lockwood, M.L. Tuttle, and G.N. Wagner, The 1986 Lake Nyos gas disaster in Cameroon, West Africa, *Science, 236*, 169-175, 1987.

Kling, G.W., W.C. Evans, M.L. Tuttle, and G. Tanyileke, Degassing of Lake Nyos, *Nature, 368*, 405-406, 1994.

Levich, V.G., *Physicochemical Hydrodynamics*, 700 pp., Prentice-Hall, Englewood Cliff, N.J., 1962.

Lorenz, V., B. Zimanowski, and G. Fröhlich, Experiments on explosive basic and ultrabasic, ultramafic, and carbonatitic volcanism, *Proceedings of the Fifth International Kimberlite Conference*, edited by H.O.A. Meyer and O.H. Leonardos, vol. 1, pp. 270-282, Companhia de Pesquisa de Recursos Minerais, Rio de Janeiro, Brazil, 1994.

Mader, H.M., J.C. Phillips, R.S.J. Sparks, and B. Sturtevant, Dynamics of explosive degassing of magma: Observations of fragmenting two-phase flows, *J. Geophys. Res., 101*, 5547-5560, 1996.

Mader, H.M., Y. Zhang, J.C. Phillips, R.S.J. Sparks, B. Sturtevant, and E.M. Stolper, Experimental simulations of explosive degassing of magma, *Nature, 372*, 85-888, 1994.

Phillips, J.C., S.J. Lane, A.M. Lejeune, and M. Hilton, Gum rosin-acetone system as an analogue to the degassing behavior of hydrated magmas, *Bull. Volcanol., 57*, 263-268, 1995.

Proussevitch, A.A., D.L. Sahagian, and A.T. Anderson, Dynamics of diffusive bubble growth in magmas: Isothermal case, *J. Geophys. Res., 98*, 22283-22307, 1993.

Sabroux, J.C., A. Villevieille, E. Dubois, C. Doyotte, M. Halbwachs, and J. Vandemeulebrouxk, Satellite monitoring of the vertical temperature profile of Lake Nyos, Cameroon, *J. Volcanol. Geotherm. Res., 42*, 381-384, 1990.

Schenker, F., and V.J. Dietrich, The Lake Nyos gas catastrophe (Cameroon): A magmatological interpretation, *Schweiz. Mineral. Petrogr. Mitt., 66*, 343-384, 1986.

Shafer, N.E., and R.N. Zare, Through a beer glass darkly, *Phys. Today, 44(10)*, 48-52, 1991.

Shaw, H.R., Viscosities of magmatic silicate liquids: An empirical method of prediction, *Am. J. Sci., 272*, 870-893, 1972.

Sigurdsson, H., J.D. Devine, F.M. Tchoua, T.S. Presser, M.K.W. Pringle, and W.C. Evans, Origin of the lethal gas burst from Lake Monoun, Cameroon, *J. Volcanol. Geotherm. Res., 31*, 1-16, 1987.

Sigvaldason, G.E., International Conference on Lake Nyos Disaster, Yaounde, Cameroon 16-20 March, 1987: Conclusions and recommendations, *J. Volcanol. Geotherm. Res., 39*, 97-107, 1989.

Sparks, R.S.J., The dynamics of bubble formation and growth in magmas: A review and analysis, *J. Volcanol. Geotherm. Res., 3*, 1-37, 1978.

Sparks, R.S.J., L. Wilson, and G. Hulme, Theoretical modeling of the generation, movement, and emplacement of pyroclastic flows by column collapse, *J. Geophys. Res., 83*, 1727-1739, 1978.

Sparks, R.S.J., J. Barclay, C. Jaupart, H.M. Mader, and J.C. Phillips, Physical aspects of magma degassing, I, Experimental and theoretical constraints on vesiculation, *Rev. Mineral., 30*, 413-445, 1994.

Steinberg, G.S., A.S. Steinberg, and A.G. Merzhanov, Fluid mechanism of pressure growth in volcanic (magmatic) systems, *Mod. Geol., 13*, 257-265, 1989a.

Steinberg, G.S., A.S. Steinberg, and A.G. Merzhanov, Fluid mechanism of pressure growth in volcanic (magmatic) systems with mass exchange, *Mod. Geol., 13*, 275-281, 1989b.

Sugioka, I., and M. Bursik, Explosive fragmentation of erupting magma, *Nature, 373*, 689-692, 1995.

Tazieff, H., Mechanisms of the Nyos carbon dioxide disaster and of so-called phreatic steam eruptions, *J. Volcanol. Geotherm. Res., 39*, 10-116, 1989.

Thomas, N., C. Jaupart, and S. Vergniolle, On the vesicularity of pumice, *J. Geophys. Res., 99*, 15633-15644, 1994.

Toramaru, A., Vesiculation process and bubble size distributions in ascending magmas with constant velocities, *J. Geophys. Res., 94*, 17523-17542, 1989.

van Wijngaarden, L., On the growth of small cavitation bubbles by convective diffusion, *Int. J. Heat Mass Transfer, 10*, 127-134, 1967.

Verhoogen, J., Mechanics of ash formation, *Am. J. Sci., 249*, 729-739, 1951.

Walker, D., and J. O. Mullins, Surface tension of natural silicate melts from 1200°-1500°C and implications for melt structure, *Contrib. Mineral. Petrol., 76*, 455-462, 1981.

Weast, R.C., *CRC Handbook of Chemistry and Physics*, pp. 2303, CRC Press, Boca Raton, Fla, 1983.

Weiss, R.F., Carbon dioxide in water and seawater: The solubility of a non-ideal gas, *Mar. Chem., 2*, 203-215, 1974.

Wiebe, R., and V.L. Gaddy, The solubility of carbon dioxide in water at various temperatures from 12 to 40° and at pressures to 500 atmospheres: Critical phenomenon, *J. Am. Chem. Soc., 62*, 815-817, 1940.

Williams, S.N., Plinian airfall deposits of basaltic composition, *Geology, 11*, 211-214, 1983.

Wilson, L., R.S.J. Sparks, T.C. Huang, and N.D. Watkins, The control of volcanic column heights by eruption energetics and dynamics, *J. Geophys. Res., 83*, 1829-1836, 1978.

Wilson, L., R.S.J. Sparks, and G.P.L. Walker, Explosive volcanic eruptions, IV, The control magma properties and conduit geometry on eruption column behavior, *Geophys. J. R. Astron. Soc., 63*, 117-148, 1980.

Wood, A.W., The dynamics of explosive volcanic eruptions, *Rev. Geophys., 33*, 495-530, 1995.

Zhang, Y., Dynamics of CO_2-driven lake eruptions, *Nature, 379*, 57-59, 1996.

Zhang, Y., and E.M. Stolper, Water diffusion in basaltic melts, *Nature, 351*, 306-309, 1991.

Zhang, Y., E.M. Stolper, and G.J. Wasserburg, Water diffusion in rhyolitic glasses, *Geochim. Cosmochim. Acta, 55*, 441-456, 1991.

E.M. Stolper, Division of Geological and Planetary Sciences, California Institute of Technology, 170-25, Pasadena, CA 91125, USA. (e-mail: ems@expet.gps.caltech.edu)

B. Sturtevant, Graduate Aeronautical Laboratories, California Institute of Technology, 301-46, Pasadena, CA 91125, USA. (e-mail: brad@galcit. caltech.edu)

Y. Zhang, Department of Geological Sciences, University of Michigan, Ann Arbor, MI 48109-1063, USA. (e-mail: youxue@umich.edu)

(Received April 12, 1996; revised September 30, 1996; accepted October 14, 1996.)